On Seismological Stress-Drop Estimates for Earthquake Sources Simulated on Rate-and-State Faults

Yen-Yu Lin[*1,2,3], Natalie Schaal[4], and Nadia Lapusta[5,6]

ABSTRACT

Seismologists estimate stress drops of small earthquakes based on specific theoretical source models. We explore the accuracy of the stress-drop estimates for several earthquake source models obtained in dynamic simulations on rate-and-state faults. We consider Madariaga-like symmetric circular sources as well as sources with directivity, elongated shapes, partial ruptures, and complex changes in the slip direction. The energy-based average stress drops computed directly on the fault for all simulated source models range from 1.5 to 5 MPa. We consider a range of focal depths and fault dips that results in 980 scenarios overall with respect to a surface network of 16 stations, where we produce synthetic waveforms assuming a known homogeneous velocity structure, and use them to obtain seismologically inferred stress drops. For the second-moment approach and spectral-fitting approach based on *S* waves and $n = 2$, the stress drops for most sources are reproduced well on average but with a significant scatter from nearly 0.01 to 100 MPa, representative of scatter for natural earthquakes, despite the actual stress-drop variation of 1.5–5 MPa. The scatter is smaller by a factor of 2 for the second-moment approach. The spectral-fitting approach based on *P* waves consistently underestimates the stress drops for noncircular sources. All approaches underestimate stress drops for ring-like sources, which leave part of the seismogenic patch unruptured. The spectral estimates are significantly affected by different averages of corner frequencies over the focal sphere for our sources versus typically assumed simple theoretical sources, as was already pointed out for some of the sources by Kaneko and Shearer (2015) and Lin and Lapusta (2018). For both second-moment and spectral methods, the scatter is amplified by partial coverage of the focal sphere by the assumed station geometry, which can also cause systematic depth-dependent artifacts.

KEY POINTS

- Stress-drop estimates use simple source models, yet physically plausible earthquake sources can be complex.
- Source complexity and network geometry result in a large artificial scatter of stress-drop estimates.
- Network geometry can introduce systematic depth-dependent artifacts in stress-drop estimates.

Supplemental Material

INTRODUCTION

Stress drop is an important source parameter for understanding earthquake physics in general and microseismicity in particular. Using generic relatively simple source models to determine stress drops of all microevents is an important and informative endeavor, and a rigorous application of such an approach that properly takes into account data quality and coverage, instrument response, and path effects is in itself a challenging research problem (Abercrombie, 1995, 2014, 2015, 2021; Hough, 1997; Ide and Beroza, 2001; Ide *et al.*, 2003; Prieto *et al.*, 2004; Shearer *et al.*, 2006; Baltay *et al.*, 2011; Lin *et al.*, 2012, 2016; Uchide and Imanishi, 2016). For a planar shear rupture in an elastic medium, the average static stress drop is proportional

1. Department of Earth Sciences, National Central University, Taoyuan, Taiwan, https://orcid.org/0000-0002-6971-3960 (Y-YL); 2. Earthquake-Disaster and Risk Evaluation and Management Center, National Central University, Taoyuan, Taiwan; 3. Graduate Institute of Applied Geology, National Central University, Taoyuan, Taiwan; 4. Department of Mechanical Engineering, California State University, Northridge, California, U.S.A., https://orcid.org/0000-0003-4825-4344 (NS); 5. Seismological Laboratory, California Institute of Technology, Pasadena, California, U.S.A., https://orcid.org/0000-0001-6558-0323 (NL); 6. Department of Mechanical and Civil Engineering, California Institute of Technology, Pasadena, California, U.S.A.

*Corresponding author: yenyulin@ncu.edu.tw

Cite this article as Lin, Y.-Y., N. Schaal, and N. Lapusta (2025). On Seismological Stress-Drop Estimates for Earthquake Sources Simulated on Rate-and-State Faults, *Bull. Seismol. Soc. Am.* **115**, 1072–1104, doi: 10.1785/0120240147

to an average slip $\bar{D}$ over a characteristic rupture length $\bar{L}$ (Kanamori and Anderson, 1975; Lay and Wallace, 1995)

$$\Delta\sigma = C\mu\left(\frac{\bar{D}}{\bar{L}}\right), \tag{1}$$

in which C is a constant that depends on the earthquake source geometry and μ is the shear modulus of the surrounding bulk. One way to determine the average slip $\bar{D}$ and characteristic length $\bar{L}$ of an earthquake is a finite-fault inversion but it is feasible only for well-recorded events.

Hence seismological estimates of average stress drop for most events are based on the seismic moment M_0 and fault dimensions called moment-base stress drop, as

$$\Delta\sigma_M = C_0\left(\frac{M_0}{A^{3/2}}\right), \tag{2}$$

in which C_0 is a constant and A is the earthquake source area (Madariaga, 1979; Noda *et al.*, 2013). The estimate is exact if the stress drop is uniform over the source and if the constant C_0 is calculated for the exact shape of the source; for a circular source, $C_0 = \frac{7}{16}\pi^{3/2} \approx 2.44$ (Madariaga, 1979; Noda *et al.*, 2013). If the stress drop is not uniform over the source, then $\Delta\sigma_M$ corresponds to averaging of the stress drop weighted by the slip distribution due to the uniform stress drop in the overall slip direction over the same ruptured domain. For a circular rupture with a constant stress drop and radius r, one has (Eshelby, 1957):

$$\Delta\sigma_M = \frac{7M_0}{16r^3}. \tag{3}$$

From analyzing the observed waveforms, seismic moment M_0 is generally well constrained, and rupture area A or radius r is approximately calculated via a series of assumptions. Stress drop is then determined from equations (2) or (3), thereby aggregating any uncertainty from A, C_0, and M_0.

To estimate the characteristic rupture dimensions or area, seismologists commonly proceed with the analyses in the frequency domain. The frequency spectrum of the displacement amplitude is fitted (Brune, 1970, 1971; Madariaga, 1976; see The spectral fitting approach section) to determine the corner frequency f_c. Then the corner frequency is converted into the source radius by assuming a circular rupture spreading from the center with a constant rupture velocity (infinite in the Brune formulation, typically 0.9β, in which β is the shear-wave speed, in the Madariaga formulation):

$$r = t_w v_R = \left(\frac{C_1}{f_c}\right)C_2\beta = \frac{k\beta}{f_c}, \tag{4a}$$

$$A = \pi r^2, \tag{4b}$$

TABLE 1
Commonly Used Spherically Averaged Values of k

Theoretical Formulation	k^P	k^S	v_R/β
Madariaga (1976)	0.32	0.21	0.9
Kaneko and Shearer (2014)	0.38	0.26	0.9
Brune (1970, 1971)	–	0.37	Infinite
Hanks and Wyss (1972)	0.64	–	Infinite
Sato and Hirasawa (1973)	0.44	0.32	0.9

in which t_w and v_R are the source duration and the constant rupture velocity, respectively. $k = C_1C_2$ is the factor between f_c and r, which is specific to a particular source model; it is essentially a normalized corner frequency, since

$$k = \frac{rf_c}{\beta}, \tag{5}$$

is nondimensional. By combining equations (3) and (4), the relationship between stress drop, corner frequency, and seismic moment is derived as follows:

$$\Delta\sigma_M = \frac{7}{16}\left(\frac{f_c}{k\beta}\right)^3 M_0. \tag{6}$$

The constant 7/16 is only appropriate for circular sources; other sources should have a different prefactor determined by their shape (e.g., Noda *et al.*, 2013).

The determination of the corner frequency f_c and the conversion factor k are nontrivial. Even for a circular source, they depend on the azimuth of the station (Sato and Hirasawa, 1973; Madariaga, 1976; Kaneko and Shearer, 2014, 2015). Because of the need to separate source, path, as well as site effects and reduce the noise, stacking is employed whereby an average corner frequency is determined and an average value of k is used to convert it to the source radius. The normalized and averaged corner frequency k is 0.37 for the S wave in the Brune formulation. For the Madariaga formulation, the average k is 0.32 and 0.21 for P and S waves, respectively, when the rupture velocity is 0.9β. The average values of k from several influential studies are presented in Table 1.

Much progress has been made in the last 30 yr or so by applying the assumption of the circular axisymmetric source to small earthquakes. The first-order issue in observational studies is to isolate the source, path, and site effects in seismic waveforms, as incomplete path and site corrections would translate into artificial changes in stress-drop scaling. In doing so, several useful approaches have been developed, such as the spectral-fitting analysis (e.g., Gibowicz *et al.*, 1991; Abercrombie, 1995; Ide *et al.*, 2003, 2004; Yamada *et al.*, 2007; Lin *et al.*, 2012; Liu *et al.*, 2023), the isolation spectra approach (e.g., Prieto *et al.*, 2004; Shearer *et al.*, 2006, 2019, 2022; Allmann and Shearer, 2007, 2009; Allmann *et al.*, 2008; Trugman and Shearer,

2017), the empirical Green's function technique (e.g., Lanza *et al.*, 1999; Ide *et al.*, 2003, 2004; Mori *et al.*, 2003; Oye *et al.*, 2005, Prieto *et al.*, 2006; Abercrombie, 20142015; Abercrombie *et al.*, 2017, 2020, ; Van Houtte and Denolle, 2018; Demuth *et al.*, 2019; Shearer *et al.*, 2019; Wu *et al.*, 2019; Shimmoto, 2022; Chang *et al.*, 2023), the asymptotic spectral ratio method (Irikura and Kamae, 1994; Miyake *et al.*, 2003; Walter *et al.*, 2017), *P* wave or source time function pulse measurement (Frankel and Kanamori, 1983; O'Neill, 1984; Lin *et al.*, 2016), and the stopping phases measurement (Imanishi and Takeo, 1998, 2002). The results generated from applying these techniques to isolate source effects indicate that stress drops are moment invariant with a large scatter from 0.1 to 100 MPa (Allmann and Shearer, 2009; Abercrombie, 2021).

Recently, there has been growing recognition that directivity and other types of source complexity are important to account for in estimating stress drops. Kaneko and Shearer (2014, 2015) numerically simulated subshear ruptures with circular and elliptical shapes, different directivity effects, and different rupture speeds and showed that the Madariaga formulation resulted in a factor of 1.4–8 difference compared to the simulated stress drops. Lin and Lapusta (2018) simulated sequences of ruptures on an asperity (patch of higher normal stress) and demonstrated that the Madariaga formulation would underestimate stress drop by two to three orders of magnitude for ring-like (i.e., hollow) earthquake sources that rupture the circumference of the asperity. Wang and Day (2017) concluded that the Madariaga formulation may overestimate stress drops by a factor of 2–4 for crack-like and pulse-like ruptures within their dynamic model. These widely varying results suggest that the stress-drop estimate is highly sensitive to the rupture characteristics.

Observations increasingly support the notion of complex, noncircular earthquake sources of all sizes. Complex source characteristics commonly appear in moderate-to-mega earthquakes as uncovered by employing finite-fault inversion approaches (e.g., Ye *et al.*, 2016a,b). Complex ruptures have also been inferred for small earthquakes (Abercrombie *et al.*, 2001, 2020; Dreger *et al.* 2007; Chen *et al.*, 2016; Kim *et al.*, 2016; Pennington *et al.*, 2022).

The second-moment approach to estimating stress drops attempts to account for some of the complexity, specifically potential directivity, and ellipticity of the rupture. It avoids averaging over different stations and instead uses the information at different stations to find an estimate of rupture length and width, and hence of rupture area (Backus and Mulcahy, 1976; Backus, 1977; Silver, 1983; Silver and Jordan, 1983; McGuire *et al.*, 2001, 2002; McGuire, 2004, 2017; Fan and McGuire, 2018; see The second-moment approach section). Of course, such an approach would only be possible assuming that the path and site effects are well known and the noise is sufficiently small.

Here, we simulate a range of earthquake sources, from Madariaga-like (MA) circular one with (nearly) constant rupture speed to rectangular (RECT) and elliptical (ELLI) sources with complex rupture scenarios, to determine the effect of rupture complexity on the accuracy of the estimated stress drop. For the MA source, we simulate just one rupture with initial conditions tailored to start the rupture in the middle of the fault and to spread in all directions with nearly constant rupture speed. For the other fault models, we simulate a sequence of earthquake ruptures, obtaining earthquake sources which are consistent with the fault geometry and constitutive assumptions and which are independent of the (arbitrary) initial conditions that we assume on the fault. From the models, we calculate the "true" value of the average stress drop on the fault and compare it to the seismologically inferred stress drops ($\Delta\sigma_{est}$) using both the spectral fitting and second-moment approaches. In our study, the path effect is negligible due to the assumption of a homogeneous purely elastic velocity structure. From these synthetic tests, we can explore the uncertainties in the seismologically estimated stress drops without path contamination.

SIMULATED EARTHQUAKE SOURCES

Fault models with rate-and-state friction

To generate rupture events, we use the 3D fault-zone dynamic modeling code, called the Boundary Integral Cycle of Earthquakes (BICyclE), developed by Lapusta and Liu (2009). A planar fault is embedded into a uniform elastic space. The fault is governed by the rate-and-state friction law (Dieterich, 1979; Ruina, 1983)

$$\tau = \sigma\left[f_o + a\ln\left(\frac{V}{V^*}\right) + b\ln\left(\frac{V^*\theta'}{D_{RS}}\right)\right], \tag{7}$$

in which τ and σ are shear and normal stress on the fault, respectively; f_o is a reference friction coefficient at the reference slip velocity V^*; a and b are constants, and V, θ', and D_{RS} are sliding velocity, state variable, and characteristic slip for the state variable evolution, respectively. We denote the state variable θ' to avoid confusion with the azimuth which is often denoted by θ. We use the aging law for state variable evolution:

$$\dot{\theta}' = 1 - \frac{V\theta'}{D_{RS}}. \tag{8}$$

In the steady-state condition of sliding with the same slip rate V, the friction coefficient in equation (7) evolves to:

$$\mu_{ss} = \mu_0 + (a-b)\ln\frac{V}{V^*}. \tag{9}$$

In fault regions with $a - b > 0$, the steady-state friction coefficient increases when sliding velocity increases, called velocity-strengthening (VS). The sliding on VS regions is stable. The friction coefficient decreases when sliding velocity increases in velocity-weakening (VW) regions where $a - b < 0$, indicating a potentially unstable seismogenic patch (Rice and Ruina,

1983; Rubin and Ampuero, 2005). The nucleation size for seismic slip in such regions, for the values of a and b that we use, is given by (Rubin and Ampuero, 2005; Chen and Lapusta, 2009; Lapusta and Liu, 2009):

$$h^* = \frac{\pi \mu^* b D_{RS}}{2\sigma(b-a)^2}, \tag{10}$$

in which σ is the normal stress, $\mu^* = \frac{\mu}{(1-\nu)}$, and ν is the Possion's ratio (0.25).

Fault models based on rate-and-state friction have been used to reproduce and study many earthquake source phenomena, including earthquake nucleation, post-seismic slip, aftershocks, and earthquake sequences, such as repeating earthquakes and patterns of seismogenic and aseismic slip (Rice, 1993; Dieterich, 1994, 2007; Ben-Zion and Rice, 1997; Lapusta *et al.*, 2000; Kaneko *et al.*, 2008; Helmstetter and Shaw, 2009; Lapusta and Liu, 2009; Barbot *et al.*, 2012; Lui and Lapusta, 2016; Lin and Lapusta, 2018). Complex sources with heterogeneous slip patterns are commonly generated due to heterogeneous physical parameters (e.g., normal stress and frictional properties) on the fault (e.g., Jiang and Fialko, 2016; Lin and Lapusta, 2018). The BICyclE code solves the constitutive law on each grid point on the fault via the spectral boundary integral method, and it is capable of long-term simulations with slow loading and spontaneous sequences of earthquakes and aseismic slip (Lapusta and Liu, 2009).

In our simulations, we vary the shape of the seismogenic, VW region (circular, RECT, or ELLI, see Fig. 1), and frictional properties of the region. However, in all models, the VW region is surrounded by a VS region and then a loading region of 40 mm/yr. The fault area of the models is 300×300 m^2 (1500×1500 cells). In some simulations, we set the area to be 300×150 m^2 (1500×750 cells) to save computational resources. The length of each computational cell is 0.2 m in both directions. The background normal stress and the reference friction coefficient are 40 MPa and 0.6, respectively. The corresponding nucleation size h^* is 10.3 m (Fig. 1a, bottom panel). The physical parameters of the dynamic modeling are given in Table 2.

Description of fault model families

We consider three source families with fault geometries that are common in seismic source studies, which are the (1) MA, (2) RECT, and (3) ELLI source families. In addition, we consider an (4) asperity-like (ASP) fault family previously studied by Lin and Lapusta (2018). We simulate one earthquake rupture for a given set of fault properties in the MA family and a sequence of 40 earthquake ruptures in the other families. Figure 2 illustrates the three MA models and Figures 3–5 show the rupture histories for the dynamic events chosen for the stress-drop analysis in this study. Forty events simulated for each fault setup (e.g., a square fault which corresponds to RECT $L/W = 1$) would be, in general, different from each other, as the prestress for each event depends on the prior slip on the fault (Fig. 4). We identify the simulated earthquake sources selected for the stress-drop analysis by the number of the corresponding event in the sequence, for example, RECT $L/W = 1$ model 9 means that the particular earthquake source occurred as event number 9 in the simulation of earthquake sequences for the RECT $L/W = 1$ fault setup.

1. The MA family

   The Madariaga model (Madariaga, 1976) is often used in seismic source studies. We generate an MA earthquake source by considering a circular VW region (diameter = 100 m) with a small area (diameter = 3 m) of a higher initial shear stress (by 5 MPa) and a smaller $D_{RS} = 2\mu$m in the center of the VW region (Fig. 1a, upper panel). In this simulation, the rupture initiates in the center of the VW region and spreads in all directions to the circular VW-VS boundary, which is consistent with the Madariaga assumptions. Because the artificial shear stress patch is needed to initiate the rupture in the center of the fault, we only simulate one event in this family (Fig. 3a) for a given set of fault properties. However, for this family only, we vary the properties of the surrounding VS region (Table 2) to study the effect of the abruptness of rupture arrest (Fig. 2): MA model 1 has the same VS properties as the other families; MA model 2 has much larger values of a and $(a - b)$ in the VS region, resulting in more abrupt arrest with the moment-rate function similar to that of the dynamic rupture in the original Madariaga (1976); and MA model 3 has much smaller values of a and $(a - b)$ in the VS regi on than MA model 1 and results in rupture penetrating significant distance into the VS region and more gradual arrest there.
2. The ELLI family

   The ELLI VW region has a major (A) and minor (I) axes. Similar to the RECT family, we consider models with $A/I = 1$ (circular), $A/I = 2$, $A/I = 4$, and $A/I = 8$ (Fig. 1c). The difference between the circular model in the ELLI source family and the MA family is the location of rupture initiation and direction of rupture propagation (Fig. 3). The earthquake source rupture in the MA family is prescribed to start in the center of the circular fault and then it spreads nearly axisymmetrically over the fault plane toward the circular boundary, similar to Madariaga (1976) and Kaneko and Shearer (2014), whereas most of the events in the ELLI family start in at the edge of the ELLI source and propagate nearly unidirectionally. In particular, ELLI $A/I = 1$ model 20 and ELLI $A/I = 2$ model 23 are similar to asymmetrical circular and asymmetrical ELLI models considered in Kaneko and Shearer (2015). Only for $A/I = 8$, the tips of the VW ellipse cannot nucleate a rupture because the width of the tip is smaller than the nucleation size in the dynamic modeling; the rupture then tends to nucleate closer to the middle of the ellipse and spread more bilaterally, which results in a different behavior than that for

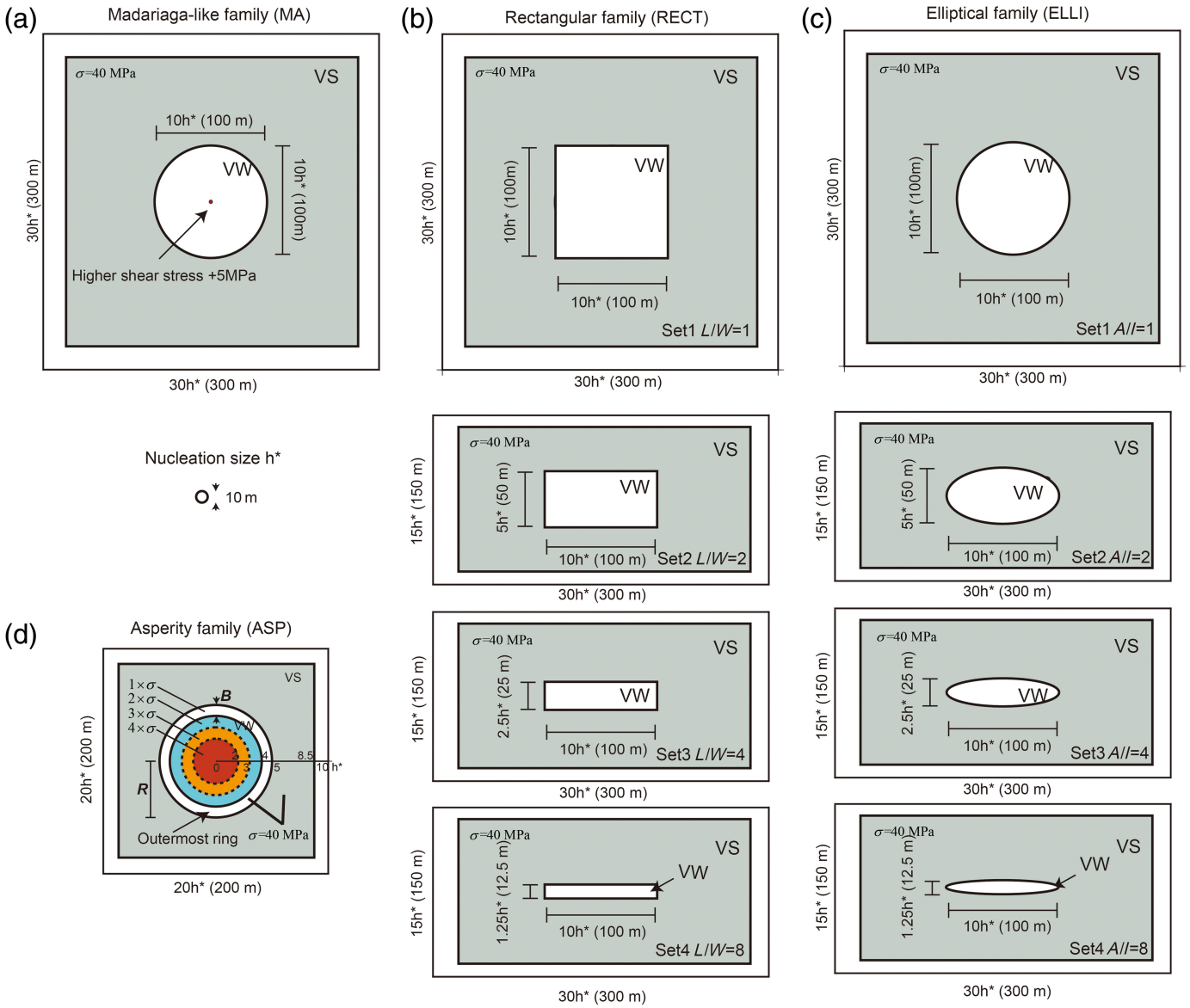

Figure 1. Schematics of the fault setup for the: (a) Madariaga-like (MA) family, (b) rectangular (RECT) family, (c) elliptical (ELLI) family, and (d) asperity-like (ASP) family. The white and gray regions indicate the velocity-weakening (VW) and velocity-strengthening (VS) areas, respectively, with the dimensions given in absolute units as well as multiples of the nucleation size h^*. The nucleation size is illustrated below in panel (a). Panel (d) is modified from figure 1(a) of Lin and Lapusta (2018). The normal stresses in the different VW regions are shown in the figure. The color version of this figure is available only in the electronic edition.

L/W = 8 from the RECT family (Figs. 3, 4). For the stress-drop analysis, we select 1, 1, 1, and 2 models from the sets of A/I = 1, A/I = 2, A/I = 4, and A/I = 8, respectively (Fig. 3).

3. The RECT family

The RECT source model is often used for describing a finite-rupture behavior, for example, in the 1D Haskell model (Haskell, 1964; Lay and Wallace, 1995). We consider four aspect ratios for this family with a fixed length (L) of 100 m and a variable width (W) of the VW region: L/W = 1 (square), L/W = 2, L/W = 4, and L/W = 8 (Fig. 1b). The rupture typically starts near the VW-VS boundary in a corner or at the edge of the RECT fault. For the stress-drop analysis, we select 3, 2, 1, and 1 models from the sets of L/W = 1, L/W = 2, L/W = 4, and L/W = 8, respectively (Fig. 4).

In both the RECT and ELLI family, most sources start in a edge of the fault and become essentially unidirectional; furthermore, sources with the aspect ratio of 4 and especially 8 are much narrower than a circular source. These nucleation locations naturally arise in our models because the nucleation occurs at the rheological boundary between the VW seismogenic region and VS barrier. Nucleating at such transitions may be common on natural faults as well. Such transitions should tend to generate streaks of microseismicity (e.g., Lapusta and Rice, 2003; Jiang and Lapusta, 2016), as observed on the Parkfield section of the San Andreas fault (e.g., Ellsworth *et al.*, 2000) and the Calaveras fault (e.g., Schaff *et al.*, 2002). In the absence of a VW-VS transition, there still

needs to be a reason for a small event to initiate and arrest, implying heterogeneity in frictional resistance or stress and hence unlikely to lead to axisymmetric circular sources. One suitable nucleation location could be a band of stress concentration due to arrest of a prior event. Microseismicity nucleating at such a location would still have reasons to propagate only into the portion of the fault that has been unruptured recently, resulting in asymmetric rupture similar to the ones we produce here. The small earthquake rupture may propagate along the band of stress concentration, resulting in a strongly elongated event. Indeed, a recent study of Ross *et al.* (2020) concluded that 63%–73% of small earthquakes exhibit unilateral ruptures.

4. The ASP family

   Here, the VW region has increasingly higher normal stress toward its center, as one would expect from compressing a bump (or asperity) on the fault interface (Lin and Lapusta, 2018). Specifically, the normal stress increases from 40 MPa along the circumference of the seismogenic region to 160 MPa in the middle. In this model, some events rupture only the circumference of the fault (ring-like sources) due to higher normal stress (and hence frictional resistance) toward the center of the patch, whereas others fully rupture the patch. For the stress-drop analysis, we chose five models (Fig. 5). Models 24 and 28 are ring-like, with an unruptured hole in the middle of the patch.

   Such physically plausible sources have some recent observational confirmation. The ASP family has been used by Lin and Lapusta (2018) to explain the observations of repeating earthquakes with similar durations but much different moments (Lin *et al.*, 2016); ring-like ruptures have similar durations but much smaller moments than ruptures of the entire patch. In another example, the last two foreshocks of the 1999 M_w 7.6 İzmit, Türkiye, earthquake had nearly identical centroids, but the first foreshock had a much lower stress drop and would be a plausible candidate for a ring-like source around an asperity that subsequently failed, extending the cascade to the nucleation of the mainshock (Ellsworth and Bulut, 2018).

TABLE 2
Physical Parameters Used in Dynamic Modeling

Parameter	Symbol	Value
Poisson's ratio	ν	0.25
Shear modulus	μ	30 GPa
S-wave speed	β	3.0 km/s
P-wave speed	α	5.2 km/s
Density	ρ	3333.3 kg/m^3
Loading rate	V_L	40 mm/yr
Rate-and-state properties in VW region	*a*	0.010
	b	0.014
Rate-and-state properties in VS region	*a*	0.019*
	b	0.014*
Reference slip velocity	*V**	10^{-6} m/s
Reference friction coefficient	f_o	0.6
Background normal stress	σ	40 MPa
Seismic velocity threshold	V_{evne}	0.1 m/s
Nucleation size for a 3D rupture	*h**	10.3 m
Characteristic length	D_{RS}	10 μm
Cell size	Δ*x*	0.2 m

*Values used in all models other than MA models 2 and 3. In MA model 2, $a = 0.050$ and $b = 0.003$. In MA model 3, $a = 0.010$ and $b = 0.009$.

Computing actual stress drop from the dynamic models

In our simulations, we can calculate the actual stress drop on the fault. We take the difference in shear stress before and after dynamic slip in each computational cell and then calculate the average stress drop on the fault.

The moment-based stress-drop averaging (formulas 2, 3, 6) is the most common in seismic studies. We obtain the moment-based stress drop $\Delta\sigma_M$ using expression (3) with the effective radius r calculated from the event rupture area A assuming a circular shape. We calculate the rupture area A by summing only the computational cells that experience a slip rate larger than the assumed seismic threshold of 0.1 m/s. One can also compute an area-based stress drop (Noda *et al.*, 2013)), which we define as

$$\Delta\sigma_A = \frac{\int_\Sigma |\underline{\Delta\sigma}| dS}{A}, \tag{11}$$

in which $\underline{\Delta\sigma}$ is the stress drop vector along the strike and dip directions at each sub-fault and Σ is the ruptured fault region. The third type of averaging results in an energy-based stress drop, which enters the expression for the strain energy change (Noda *et al.*, 2013). We compute it as

$$\Delta\sigma_E = \frac{\int \underline{\Delta\sigma} \cdot \underline{\Delta u} dS}{\int |\underline{\Delta u}| dS}, \tag{12}$$

in which $\underline{\Delta u}$ is the slip vector along the strike and dip directions at each subfault. The dot symbol indicates the dot product. This stress drop average is weighted by the final slip distribution.

WAVEFORM SIMULATION AND ESTIMATION OF SEISMOLOGICALLY INFERRED STRESS DROP ($\Delta\sigma_{est}$)

Waveform calculation

We follow the procedure of computing the waveform synthetics from Lin and Lapusta (2018) and simulate far-field displacement seismograms for the dynamic sources in the homogeneous elastic whole spaces. For each cell, the displacements are given by:

$$u(x,t) = \frac{1}{4\pi\rho\alpha^3} R^P \frac{1}{d} \dot{M}_0\left(t - \frac{d}{\alpha}\right) + \frac{1}{4\pi\rho\beta^3} R^S \frac{1}{d} \dot{M}_0\left(t - \frac{d}{\beta}\right), \tag{13}$$

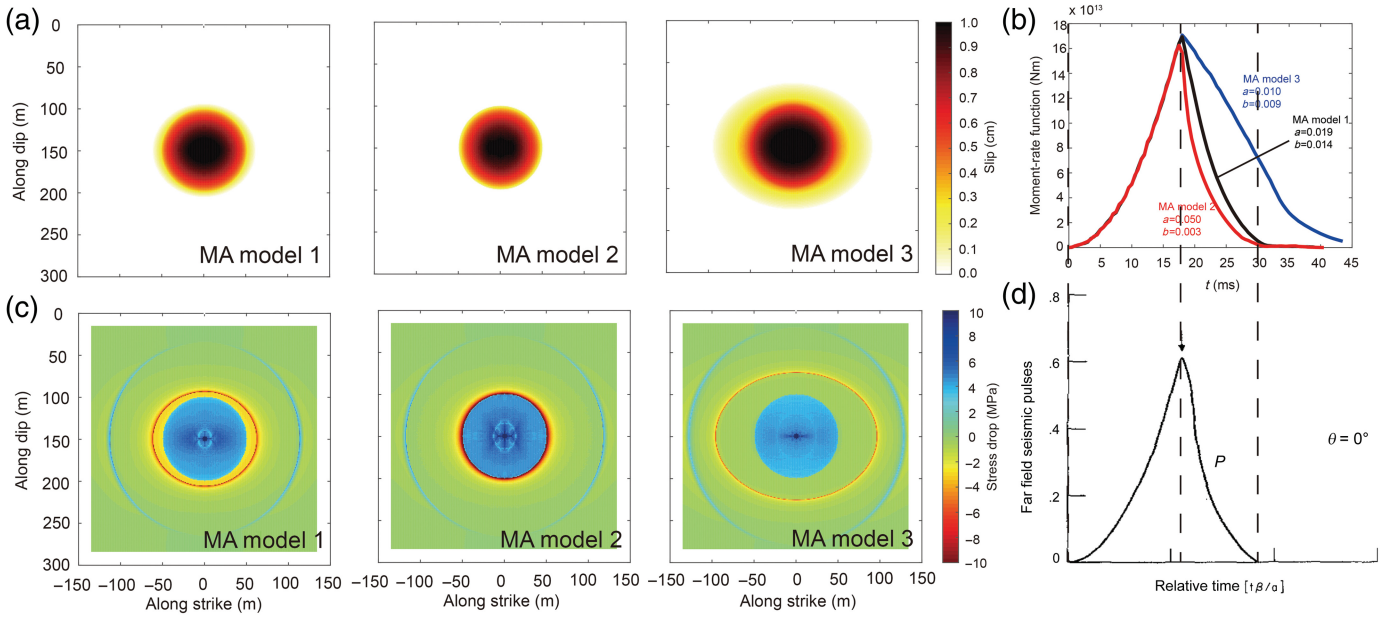

Figure 2. Three MA models with different properties of the arresting VS region and hence different abruptness of arrest: MA model 1 has the same VS properties as the rest of the families, MA model 2 has more VS properties and more abrupt arrest, and MA model 3 has less VS properties and hence penetrates the VS region with more gradual arrest. (a) Slip distributions for the three MA models. (b) Moment-rate functions of the MA models 1–3 (black, red, and blue lines, respectively). (c) Distributions of stress drop for the three models. The boundary of the seismically ruptured region is visible as the red contour of stress concentration at the location of the rupture arrest. (d) The simulated far-field *P*-wave displacements from the work of Madariaga (1976) are proportional to the moment-rate function. This panel is modified from figure 9 of Madariaga (1976). The comparison of panels (b) and (d) shows that our MA model 2 is very similar in terms of the abruptness of arrest and general waveform shape to the source considered in Madariaga (1976), and MA model 1 is also close. MA model 3 has a much more gradual arrest and hence a wider waveform.

in which ρ is the density, $\dot{M}_0$ is the moment-rate function, d is the distance from the earthquake source to receiver x, and R^P and R^S are the radiation patterns of far-field P and S waves, respectively (modified from eq. 4.32 of Aki and Richards, 2002). To consider a finite source, we sum contributions from several sub-faults (i.e., the ruptured cells). It is important that we do not consider any path effects (e.g., attenuation and site effects) in this the synthetic waveform approach. This is by design, so that our synthetics reveal pure source effects.

The spectral-fitting approach

In the spectral-fitting analysis, the path- and receiver-corrected displacement amplitude spectrum is fitted by:

$$S(f) = \frac{\Omega_0}{[1 + (f/f_c)^{\gamma n}]^{1/\gamma}}, \tag{14}$$

in which Ω_0 is the amplitude level in the low-frequency portion related to the seismic moment, f_c is the corner frequency inversely proportional to the source duration, n is related to the fall-off rate in the high-frequency portion of the spectrum, and γ is a constant controlling the shape of the corner (Aki, 1967; Brune, 1970; Boatwright, 1980). The commonly used Brune ω^{-2} source model corresponds to $n = 2$ and $\gamma = 1$; the Boatwright ω^{-2} source model corresponds to $n = 2$ and $\gamma = 2$. Some theoretical source models predict an ω^{-3} fall-off rate ($n = 3$) at high frequencies (Aki, 1967; Hanks, 1979). The rupture duration, source size, and moment-based stress drop can be estimated from the average corner frequency f_c and seismic moment M_0 using formula (6) as discussed in the Introduction.

In the present study, we follow the procedure of the spectral-fitting approach described in Lin and Lapusta (2018), which is done in the log–log domain (Text S1, available in the supplemental material to this article), and use two theoretical spectra for fitting: (1) the Brune ω^{-2} source spectrum ($n = 2$, $\gamma = 1$) and (2) the source spectrum with n being another fitted parameter ($n = ?$, $\gamma = 1$). The fitting range is from 1 to 100 Hz as applied in observations for small earthquakes in deep boreholes (Abercrombie, 1995; Lin *et al.*, 2012), although a maximum of 20–40 Hz is more typical surface stations (Abercrombie, 2021, and references therein). More details are given in Text S1, with the fit errors and examples shown in Figures S1 and S2. For the bulk of the study, we use a set of 16 stations of limited spatial extent on a flat surface as described in the Scenarios for stations on the surface section. In the Discussion and Conclusions section, we comment on the changes when a smaller subset of eight stations is used. We fit the waveforms at each station

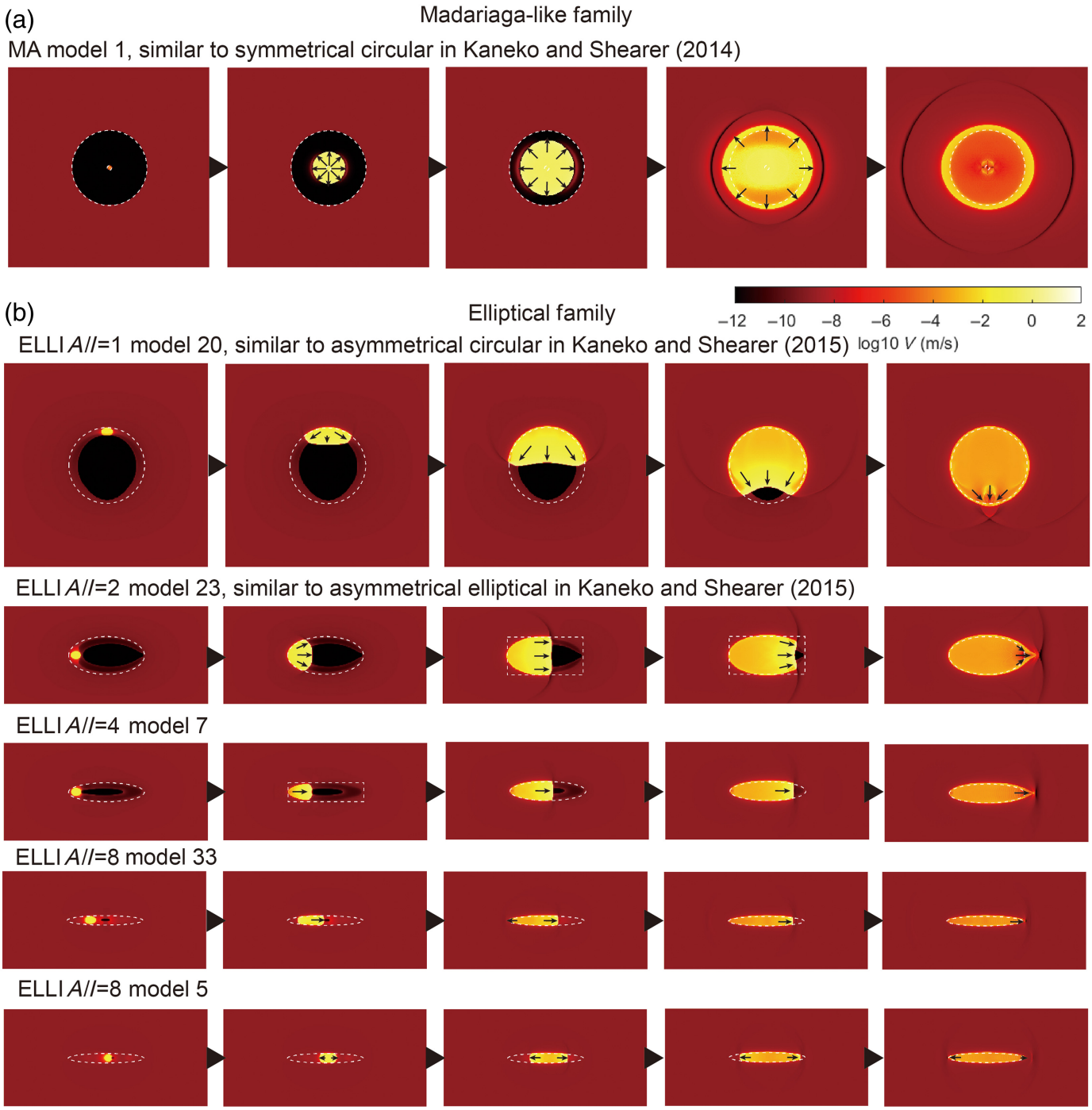

separately, and then find the average corner frequency for all stations by averaging the corner frequencies obtained at each station.

For the computation of the distribution of k values for the entire focal sphere, we take the corner frequency f_c determined from the fit at a particular location and use formula (5) to determine k, with $r = \sqrt{A/\pi}$, in which A is the actual area of our source, as done in Kaneko and Shearer (2015). For the circular source, r would be its radius. For a source of a different shape, r would represent the radius of a circle with the same source area.

Figure 3. Rupture history of the earthquake source models simulated in (a) the MA family and (b) the ELLI family and chosen for the stress drop analysis. The color indicates the slip rate on the fault on a log scale. The dashed white lines indicate the boundary of the VW-VS region. The arrows show rupture directions during the propagation. MA model 1, ELLI $A/l = 1$ model 20, and ELLI $A/l = 2$ model 23 are similar to symmetrical circular, asymmetrical circular, and asymmetrical ELLI models considered in Kaneko and Shearer (2014, 2015). The color version of this figure is available only in the electronic edition.

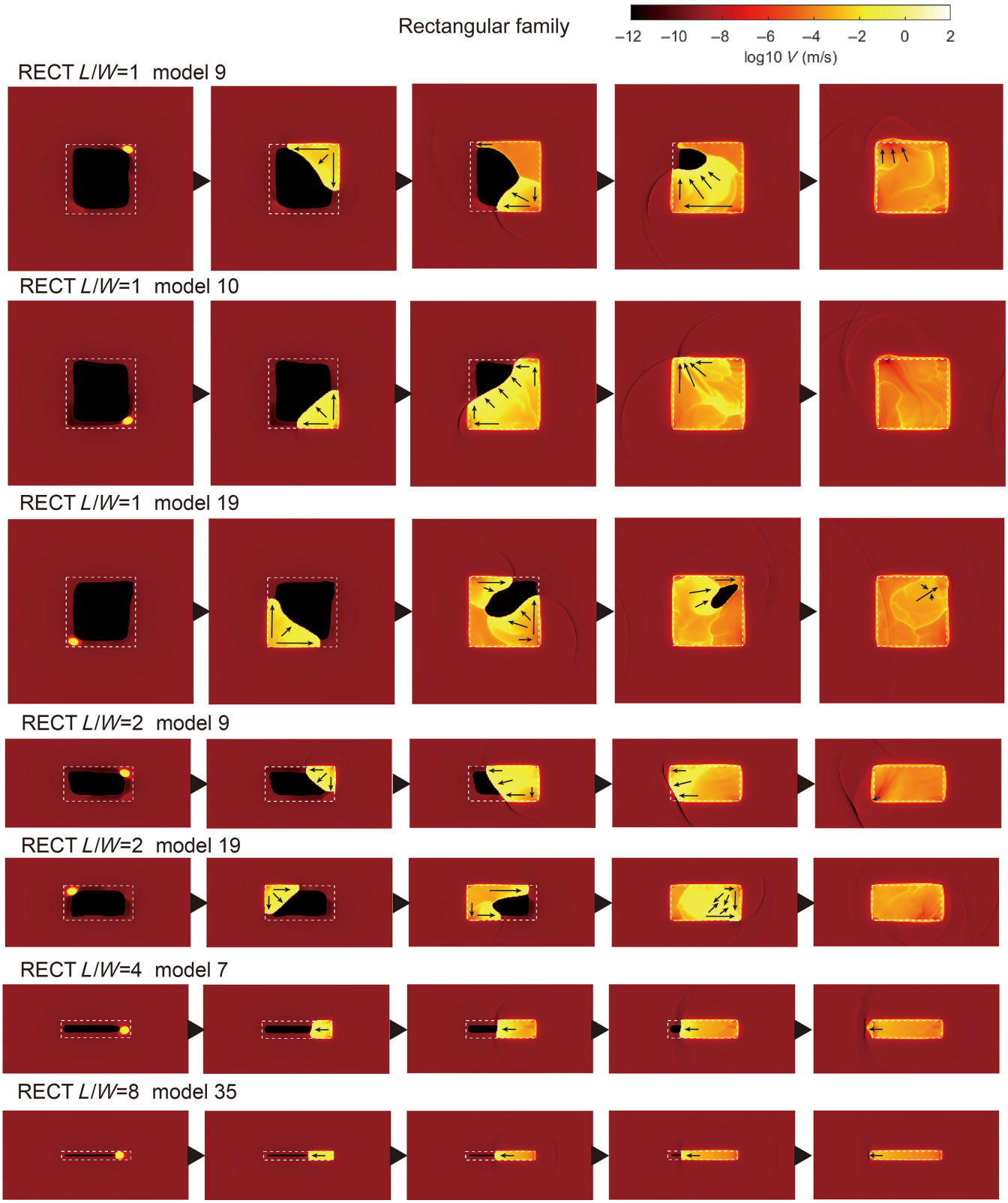

The second-moment approach

The second moments of the slip-rate distribution include information about the spatial and temporal extent of the rupture and its directivity. If one assumes that the moment-rate rate tensor is described by:

Figure 4. Rupture history of the source models in the RECT family chosen for the stress-drop analysis. The color indicates the slip rate on the fault on a log scale. The white dashed lines demonstrate the boundary of the VW–VS region. The arrows show rupture directions during the propagation. The color version of this figure is available only in the electronic edition.

$$\dot{\underline{\underline{M}}}(\underline{r},t) = \dot{\underline{\underline{M}}}\dot{f}(\underline{r},t), \tag{15}$$

in which $\dot{\underline{\underline{M}}}$ is a unit-norm moment tensor and $\dot{f}(\underline{r},t)$ is a scalar function, the second moments are defined as follows:

$$\hat{\underline{\underline{\mu}}}^{(2,0)} = \iint \dot{f}(\underline{r},t)(\underline{r}-\underline{r}_0)(\underline{r}-\underline{r}_0)dVdt, \tag{16a}$$

$$\hat{\underline{\mu}}^{(1,1)} = \iint \dot{f}(\underline{r},t)(\underline{r}-\underline{r}_0)(t-t_0)\mathrm{d}V\mathrm{d}t, \tag{16b}$$

$$\hat{\mu}^{(0,2)} = \iint \dot{f}(\underline{r},t)(t-t_0)(t-t_0)\mathrm{d}V\mathrm{d}t, \tag{16c}$$

in which $\underline{r}_0$ and t_0 denote the centroid location and time (i.e., the first moments), respectively (Backus and Mulcahy, 1976; Backus, 1977; Silver, 1983; Silver and Jordan, 1983; McGuire *et al.*, 2001).

The characteristic rupture duration τ_c, the spatial extent of the rupture, and the average propagation velocity $\underline{v}_0$ of the instantaneous spatial centroid can be determined from the second moments (Backus and Mulcahy, 1976; Backus, 1977; Silver, 1983; Silver and Jordan, 1983; McGuire *et al.*, 2001)

$$x_c(\hat{\underline{n}}) = 2\sqrt{\hat{\underline{n}}^T\hat{\underline{\underline{\mu}}}^{(2,0)}\hat{\underline{n}}}, \tag{17a}$$

$$\tau_c = 2\sqrt{\hat{\mu}^{(0,2)}}, \tag{17b}$$

$$v_c = L_c/\tau_c, \tag{17c}$$

$$\underline{v}_0 = \hat{\underline{\mu}}^{(1,1)}/\hat{\mu}^{(0,2)}, \tag{17d}$$

in which $x_c(\hat{\underline{n}})$ is the spatial extent of the rupture in the direction $\hat{\underline{n}}$ and L_c is the rupture length, which is equal to the largest eigenvalue of $\hat{\underline{\underline{\mu}}}^{(2,0)}$. The second-largest eigenvalue of $\hat{\underline{\underline{\mu}}}^{(2,0)}$ gives the rupture width W_c. To find the second moments in practice, one can use the relation between the second moments and the azimuthal variations in the apparent duration $\mu^{(0,2)}(\underline{s})$ at a given station as

$$\mu^{(0,2)}(\underline{s}) = \hat{\mu}^{(0,2)} - 2\underline{s}\cdot\hat{\underline{\mu}}^{(1,1)} + \underline{s}\cdot\hat{\underline{\underline{\mu}}}^{(2,0)}\cdot\underline{s} \tag{18}$$

in which $\mu^{(0,2)}(\underline{s})$ is measured at each station and $\underline{s}$ presents the slowness of a given phase in the source region (Silver, 1983; McGuire, 2004, 2017; McGuire and Kaneko, 2018). The dot symbol indicates the dot product. In the present study, we assume that far-field P waves are proportional to the apparent source time function. Thus, we consider P-wave durations to be the apparent durations corresponding to the inputs of $\mu^{(0,2)}(\underline{s})$. The duration is measured by the same method in McGuire (2017).

We follow the procedure from McGuire (2017) to use relationships (17, 18) to estimate stress drops based on second moments. We modify the MATLAB codes developed in McGuire (2017) and invert for the second moments on the well-known 2D nodal plane of an earthquake since our sources are well-defined and use P-wave synthetic seismograms to determine $\mu^{(0,2)}(\underline{s})$. Based on $\mu^{(0,2)}(\underline{s})$ from our observation stations described in the Scenarios for stations on the surface section, we find the second moments using equation (18) and the corresponding estimates of the synthetic earthquake source properties using equation (17). We then estimate the source rupture area by

$$A = \pi L_c W_c, \tag{19}$$

and the stress drop by formula (2) using $C_0 = 2.44$.

Scenarios for stations on the surface

To replicate practical constraints of seismic observations for natural faults, we place 16 pseudostations on a flat surface (rather than on a spherical surface as in theoretical studies) and with a limited spatial extent 60×60 km^2 (Fig. 6a). The spatial interval between the closest stations is 20 km; the distance H between the epicenter and the furthest station is 42.4 km (Fig. 6). The geometry of a source and stations and the spectral-fitting results are similar to figure 2(b) and 2(f-g) in Lin and Lapusta (2018), respectively. Here, we consider (1) a variable dip of the sources with 0.0°, 15.0°, 30.0°, 45.0°, 60.0°, 75.0°, and 90.0° (Fig. 6b) as well as (2) variable depth D of the sources that results in D/H = 0.125, D/H = 0.25, D/H = 0.5, D/H = 1, D/H = 2, D/H = 4, and D/H = 8, corresponding to the depths of 5.3, 10.6, 21.2, 42.4, 84.8, 169.6, and 339.2 km, respectively. This depth range covers common depths for earthquakes that are observed on natural faults, including deep events. In total, we have 980 scenarios comprised of combinations of different rupture models (simulated in our rate-and-state fault models as described in the Description of fault model families section), dip angles, and event depths; each source is assumed to have a right-lateral slip (rake = 180°). In each scenario, we calculate four estimates of stress drop from the spectral-fitting approach using P or S waves and considering n = 2 or fitting for n in the inversion (which we call "n fitted" or "n = ?" in the following) as described in The spectral-fitting approach section, as well as one estimate from the second-moment approach as described in The second-moment approach section. Consequently, we generate 4900 estimates of $\Delta\sigma_{\mathrm{est}}$ as shown in Table S1.

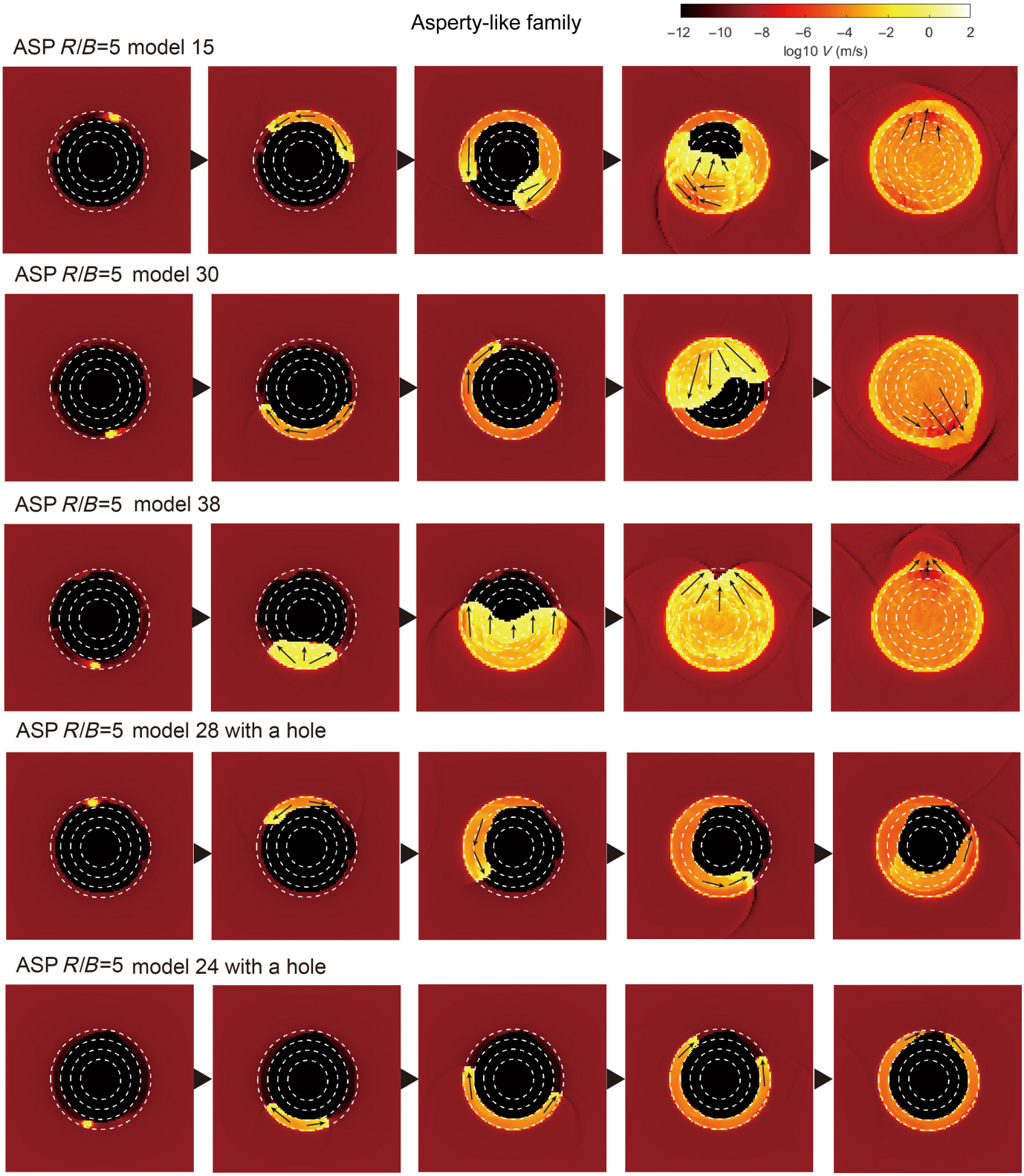

ACTUAL AND ESTIMATED STRESS DROPS FOR ALL SOURCE MODELS

Stress drops from the dynamic models

The advantage of dynamic modeling is that we can evaluate source parameters (e.g., stress and slip) from direct measurements of the simulated fault (Table 3). Most of the average

Figure 5. Rupture history of the sources models in the ASP family chosen for the stress-drop analysis. The color indicates the slip rate on the fault on a log scale. The white-dashed lines indicate the boundary of the VW–VS region and the boundaries between regions of different normal stress. The arrows show rupture directions during the propagation. The color version of this figure is available only in the electronic edition.

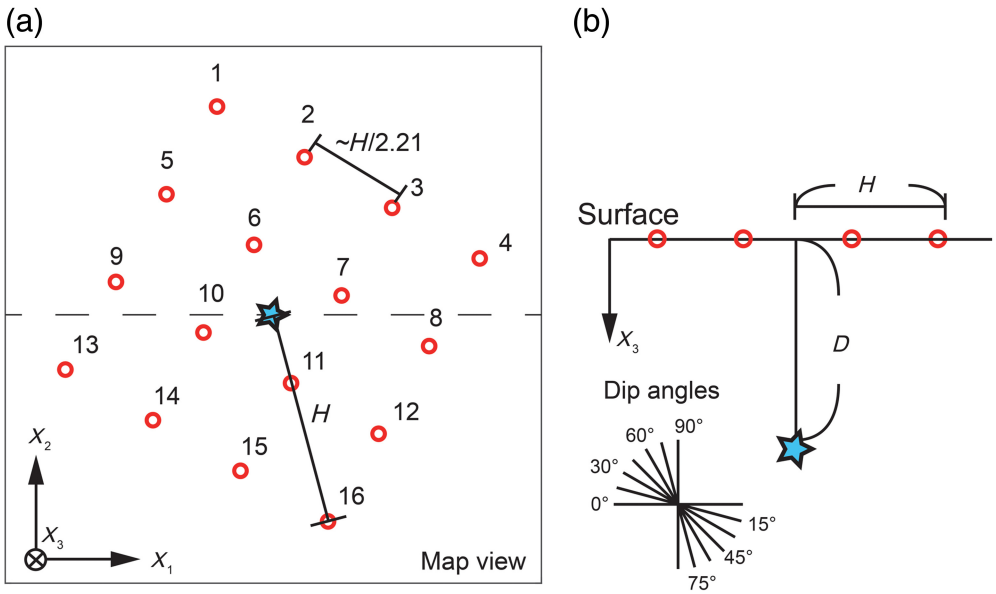

Figure 6. (a) A map view and (b) a vertical profile of the source-station geometry. The circles are the pseudostations. The stars are the epicenter and hypocenter in panels (a) and (b), respectively. *D* and *H* are the depth of the source and the maximum epicenter distance for the stations, respectively. We consider different fault-plane dip angles from 0° to 90° with a 15° interval in the scenarios and different *D*/*H* from 1/8 to 8. For *H* of 42.4 km considered here, the depth values considered are 5.3, 10.6, 21.2, 42.4, 84.8, 169.6, and 339.2 km. The color version of this figure is available only in the electronic edition.

stress drops range from 1.5 to 4 MPa for all averaging methods described in the Computing actual stress drop from the dynamic models section (Fig. 7), which is consistent with observations of natural earthquakes most of which have stress drops around ~3 MPa (Kanamori and Anderson, 1975; Allmann and Shearer, 2009; Abercrombie, 2021). The three average measures of stress drops are virtually identical for the MA models 1 and 2, as expected theoretically because the source has a near-constant spatial distribution of static stress change (Fig. 2), which should average to the same value (e.g., Noda *et al.*, 2013).

For our source models, the area-based stress-drop estimate $\Delta\sigma_A$ is generally similar to the energy-based $\Delta\sigma_E$, except for the MA model 3 which shows a larger difference (still less than a factor of 2). The similarity between these two stress-drop measures indicates that most of our simulated sources have relatively homogeneous stress-drop distributions, as heterogeneities in stress drop and slip would result in differences between the two measures (Noda *et al.*, 2013). The larger difference for the MA model 3 is due to the more gradual arrest in the VS region for that source model (Fig. 2), which results in a more heterogeneous stress drop of about 4 MPa in the circular VW region and about −0.5 MPa (stress increase by about 0.5 MPa) in the surrounding ELLI area within the VS region that also experiences seismic slip (of much smaller magnitude). This stress-drop distribution averages 1.8 MPa for the unweighted area average (equation 11) and 2.7 MPa when the stress drop is weighted by the slip in the energy-based averaging (equation 12).

The moment-based stress drop $\Delta\sigma_M$ is smaller than $\Delta\sigma_E$ when the rupture width of the models is much shorter than the length, such as the RECT $L/W = 8$ model, the ELLI $A/I = 8$ models, and ASP $R/B = 5$ models 24 and 28. The discrepancy for these sources ranges from a factor of 1.5–3. The main reason is likely that we use the factor $C_0 = 2.44$ in equation (2) from a circular crack model with a constant stress drop, and the factor would be different for sources of other shapes; for example, $C_0 = 2.53$, 3.02, and 5.21 for RECT sources with aspect ratios 1, 4, and 16, respectively (Noda *et al.*, 2013). However, the shape of the source is often unknown in practice. Because of that, as well as for its value in energy balance (e.g., Noda *et al.*, 2013), in the following, we use the energy-based stress drop $\Delta\sigma_E$ as the "true" stress drop for comparisons with $\Delta\sigma_{est}$. In addition, elongated sources result in pulse-like ruptures due to their confinement by width. $\Delta\sigma_M$ and $\Delta\sigma_E$ are similar if there is not much difference between rupture length and width and fault properties are uniform, cases which produce crack-like ruptures. Hence our results are similar to those of Wang and Day (2017), which reported that the $\Delta\sigma_E$ is larger than $\Delta\sigma_M$ for the pulse-like rupture, and there is no difference in both stress drops for the crack-like rupture. Because the second-moment and spectral methods aim to estimate $\Delta\sigma_M$, we have to keep in mind that $\Delta\sigma_M$ is a lower bound for the energy-based stress drops $\Delta\sigma_E$ that are needed for energy considerations (e.g., Noda *et al.*, 2013). The energy-based stress drops can be seismologically estimated from finite-fault inversions (Ye *et al.*, 2016a,b).

Stress-drop estimates $\Delta\sigma_{est}$ from the synthetic waveforms

The $\Delta\sigma_{est}$ for all scenarios are shown in Figure 8, and all estimates of source parameters are shown in Table S1. For most sources, the stress-drop estimates by the second-moment approach concentrate near the true stress-drop range from 1.5 to 4 MPa (the gray strip in Fig. 7). For the two ASP models (models 24 and 28), the second-moment estimates are significantly lower, at 0.07 and 0.3 MPa than the actual energy-based

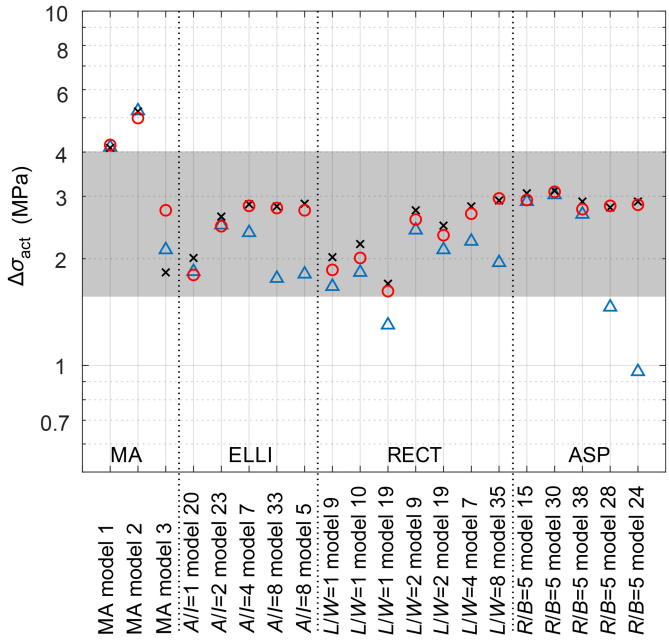

Figure 7. Average stress drops estimated directly from the on-fault dynamic models: Moment-based $\Delta\sigma_M$ (triangles), area-based $\Delta\sigma_A$ (crosses), and energy-based $\Delta\sigma_E$ (circles). The gray strip marks the range of $\Delta\sigma_E$ (1.5–4 MPa) for all models. The color version of this figure is available only in the electronic edition.

stress drops of about 3 MPa and moment-based ones of about 1 and 1.5 MPa, respectively. These are the two source models in our study that are ring-like, with an unruptured area ("hole") in the middle, so it is expected that the second moment would not be able to estimate the area of such sources well, as we discuss more in the Discrepancies Between Actual and Estimated Stress Drops in Our Study and Factors Affecting Them section.

The spectral-fitting approach with P waves for both $n = 2$ and n fitted significantly underestimates stress drops for all models except the MA models 1–3. The results from the spectral fitting approach with S waves for both $n = 2$ and n fitted show strong model-dependent bias in stress-drop calculations. In general, the $\Delta\sigma_{est}$ values, regardless of the applied approach, vary from 0.01 to 100 MPa, which is similar to the general range of estimated stress drop reported in Allmann and Shearer (2009) and Abercrombie (2021). Our results show that the stress drops for a number of our sources are significantly underestimated, the implications of which we discuss in more detail in the Discussion and Conclusions section.

We find that these significant differences between the actual and estimated stress drops for the spectral methods are mainly related to using incorrect values of k in formula (6), as also shown in previous studies (e.g., Kaneko and Shearer, 2015; Lin and Lapusta, 2018). Because often done for natural

TABLE 3
Source Parameters Computed Directly from the Simulated Dynamic Models

Family (Set)	Event Number*	M_w	M_0 (N·m)	A (m^2)	δ (cm)	v_R/β	t_w (s)	$\Delta\sigma_A$ (MPa)	$\Delta\sigma_M$ (MPa)	$\Delta\sigma_E$ (MPa)
MA model 1	1†	2.10	1.8×10^{12}	10,423	0.57	0.92	0.039	4.11	4.13	4.19
MA model 2	1†	2.05	1.5×10^{12}	7,977	0.64	0.93	0.041	5.21	5.23	4.99
MA model 3	1†	2.24	2.9×10^{12}	22,315	0.43	0.89	0.044	1.83	2.12	2.74
ELLI (A/I = 1)	20	1.77	5.7×10^{11}	8,250	0.23	0.77	0.055	2.01	1.84	1.80
ELLI (A/I = 2)	23	1.57	2.9×10^{11}	4,274	0.22	0.82	0.045	2.63	2.49	2.47
ELLI (A/I = 4)	7	1.26	9.7×10^{10}	2,143	0.15	1.10	0.041	2.85	2.37	2.82
ELLI (A/I = 8)	33	0.85	2.3×10^{10}	1,017	0.08	1.07	0.028	2.81	1.76	2.78
ELLI (A/I = 8)	5	0.86	2.4×10^{10}	1,021	0.08	0.88	0.024	2.86	1.81	2.74
RECT (L/W = 1)	9	1.86	7.6×10^{11}	10,710	0.24	0.70	0.106	2.02	1.67	1.86
RECT (L/W = 1)	10	1.89	8.5×10^{11}	10,874	0.26	0.75	0.081	2.20	1.83	2.01
RECT (L/W = 1)	19	1.77	5.6×10^{11}	10,366	0.18	0.63	0.108	1.70	1.3	1.62
RECT (L/W = 2)	9	1.67	4.0×10^{11}	5,516	0.24	0.81	0.052	2.74	2.41	2.58
RECT (L/W = 2)	19	1.63	3.5×10^{11}	5,466	0.21	0.66	0.063	2.48	2.12	2.33
RECT (L/W = 4)	7	1.36	1.3×10^{11}	2,780	0.16	0.80	0.041	2.81	2.24	2.68
ASP (L/W = 8)	35	1.00	3.9×10^{10}	1,338	0.10	1.00	0.035	2.92	1.95	2.96
ASP (R/B = 5)	15	1.98	1.1×10^{12}	9,744	0.39	0.67	0.091	3.06	2.90	2.93
ASP (R/B = 5)	30	1.99	1.2×10^{12}	9,764	0.40	0.73	0.112	3.11	3.03	3.09
ASP (R/B = 5)	38	1.94	9.9×10^{11}	9,372	0.35	0.77	0.060	2.90	2.67	2.76
ASP (R/B = 5)	28	1.43	1.7×10^{11}	4,360	0.13	0.76	0.093	2.79	1.46	2.82
ASP (R/B = 5)	24	1.08	5.2×10^{10}	2,604	0.07	0.80	0.057	2.90	0.96	2.84

ASP, asperity-like; ELLI, elliptical; MA, Madariaga-like; RECT, rectangular.
*Event number gives the number of events chosen for the stress-drop analysis out of the sequence of 40 events generated for each family other than Madariaga-like (MA). We then use this number to identify the corresponding earthquake source model, for example, RECT (L/W = 1) model 9.
†For the MA family, one event is generated per each set of fault properties.

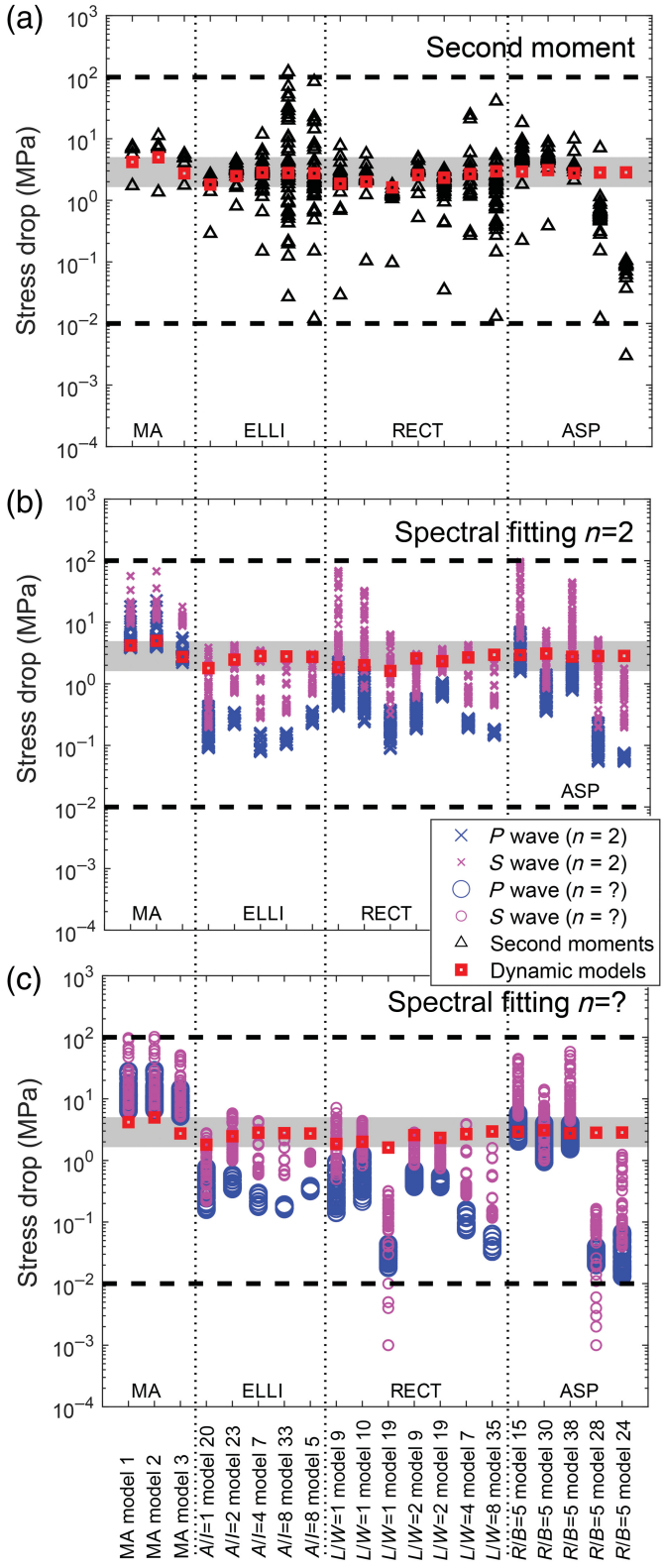

Figure 8. Seismologically estimated stress drops ($\Delta\sigma_{est}$) for all models from (a) the second-moment approach, (b) the spectral-fitting approach (n = 2), and (c) the spectral-fitting approach (n fitted). The description of symbols is shown in the figure legends. The dashed lines show the general range of estimated stress drop from 0.01 to 100 MPa. The gray area is the range of the actual stress drops $\Delta\sigma_E$ (1.5–4 MPa) for all models, with the red square indicating the actual stress drop for each model.

earthquakes, we use the average values of k reported in Madariaga (1976) to obtain the seismological estimates. The values of k for our dynamically simulated sources can be significantly different (Fig. 9, 10), as we discuss in the Discrepancies Between Actual and Estimated Stress Drops in Our Study and Factors Affecting Them section. The average values of k for our dynamically simulated earthquake sources are compared to the ones from Madariaga (1976) in Figure 11, which also shows the average values of n for the n-fitted approach and k^P/k^S ratios. The average fitting residuals (ER) and examples of the fit are shown in Figures S1 and S2 (Text S1). Although ERs for the n = 2 approach are slightly larger than for the n-fitted approach, we find that the fitting results are still acceptable (Fig. S2). We calculate the spherically averaged k values using the spherical Fibonacci grids for 824 stations (Swinbank and Purser, 2006; Marques *et al.*, 2019), to set an equal station spatial density on the entire focal sphere (Text S2; Figs. S3, S4; Table 4). This is different from Madariaga (1976), for which the average k was computed by weighting by the angle between the fault normal to seismic ray to station ζ. We see that the spherically averaged k^S for the S waves using n = 2 concentrates near the dashed line of $k^S = 0.21$ from Madariaga (1976), but the other values have more discrepancy, especially for the P waves (Fig. 9).

To further analyze $\Delta\sigma_{est}$ obtained for different source families as well as different source depth and fault dip, we show histograms of $\Delta\sigma_{est}/\Delta\sigma_E$ for a number of scenarios in Figures 12–14. We define the following measure of the difference between the seismological estimates and the actual stress drops:

$$bias = \log_{10}\left(\frac{\Delta\sigma_{est}}{\Delta\sigma_E}\right), \tag{20}$$

which is given on the top axis of Figures 10 and 11. We calculate the mean and median absolute deviation (MAD) of *bias* for all models (Table 5). In the following, we, in part, characterize the uncertainty of the approaches based on the mean of the *bias* and then assess the scattering of results by MAD of the *bias* because MAD would not be affected by extreme values.

DISCREPANCIES BETWEEN ACTUAL AND ESTIMATED STRESS DROPS IN OUR STUDY AND FACTORS AFFECTING THEM

Stress-drop estimates for the MA family

Our MA sources have been specifically added to consider the best-case scenario for the stress-drops estimation; hence it is instructive to consider the results in detail. One might expect that the estimated stress drops would be closest to the actual ones for this family overall. This is true in relation to the spread of the stress drops, which is the smallest from all source families, with all estimated values overall differing not much more than 10 times from the actual values. However, surprisingly, we find that all approaches overestimate stress drops for the MA

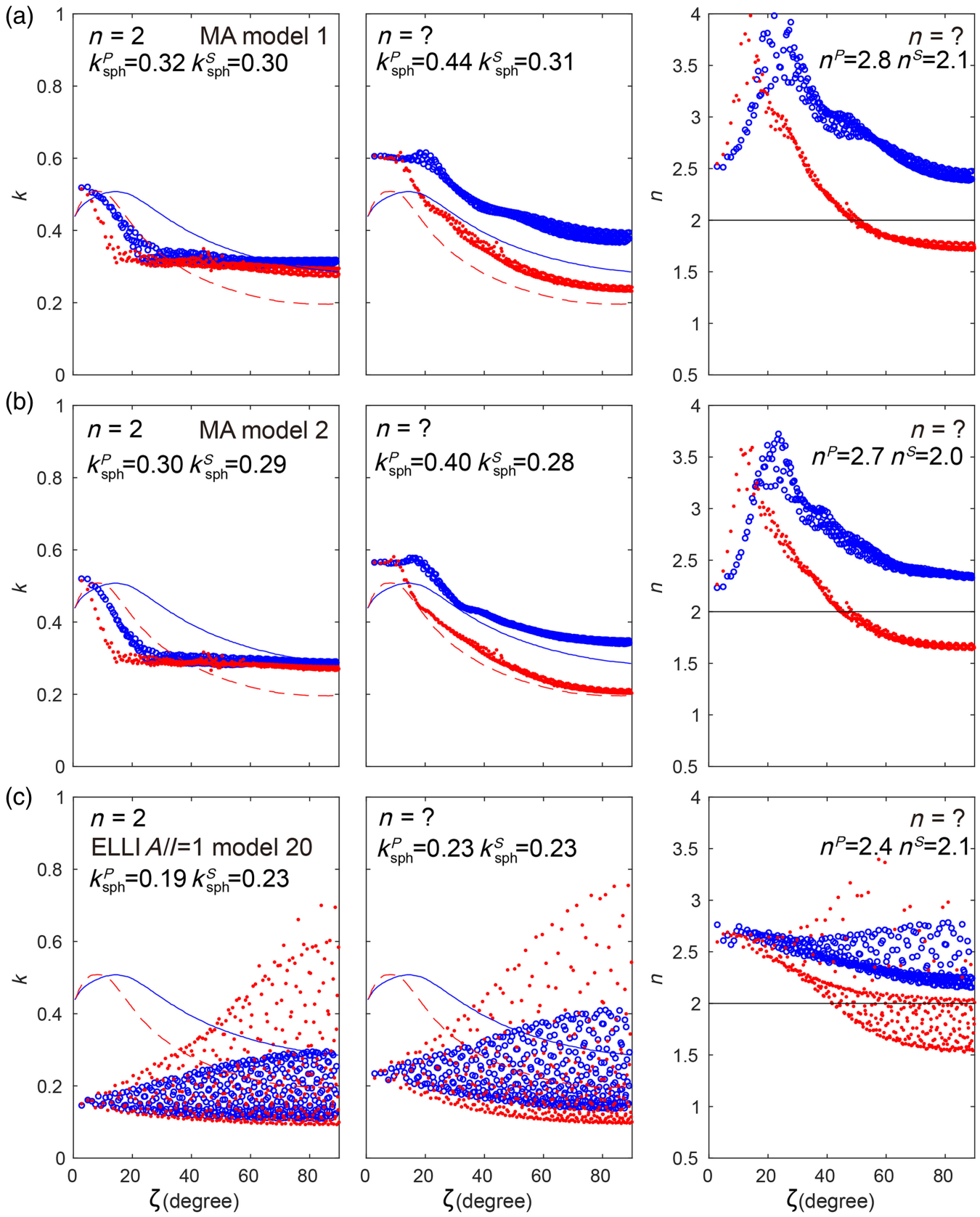

Figure 9. Values of k computed from our synthetic seismograms versus ζ for (a) MA model 1, (b) MA model 2, and (c) ELLI $A/\!/ = 1$ model 20 (which is similar to asymmetrical circular model of Kaneko and Shearer, 2015). Circles and dots are actual k^P and k^S, respectively, for all stations on a focal sphere. Solid and dashed lines are k^P and k^S, respectively, from the axisymmetric circular Madariaga model (Madariaga, 1976). The average k^P and k^S from the focal sphere are mentioned in the figure as k^P_{sph} and k^S_{sph}, respectively. The color version of this figure is available only in the electronic edition.

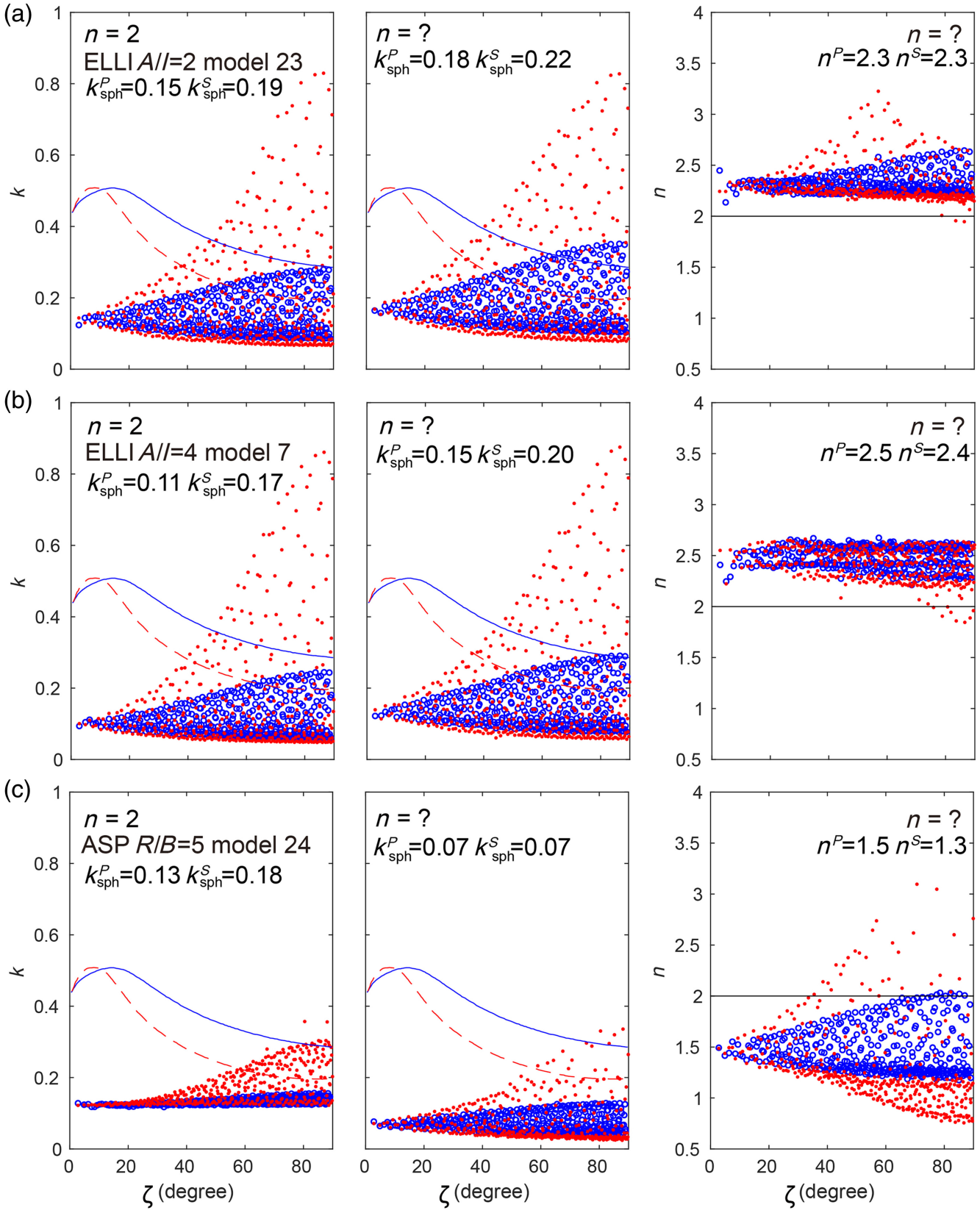

Figure 10. Values of k computed from our synthetic seismograms versus ζ for (a) ELLI $A/\!/ = 2$ model 23 (which is similar to the asymmetrical ELLI model of Kaneko and Shearer, 2015), (b) the ELLI $A/\!/ = 4$ model 7, and (c) the ASP $R/B = 5$ model 24. Circles and dots are actual k^P and k^S, respectively, for all stations on a focal sphere. Solid and dashed lines are k^P and k^S, respectively, from the axisymmetric Madariaga model (Madariaga, 1976). The average k^P and k^S from the focal sphere are mentioned in the figure as k^P_{sph} and k^S_{sph}, respectively. The color version of this figure is available only in the electronic edition.

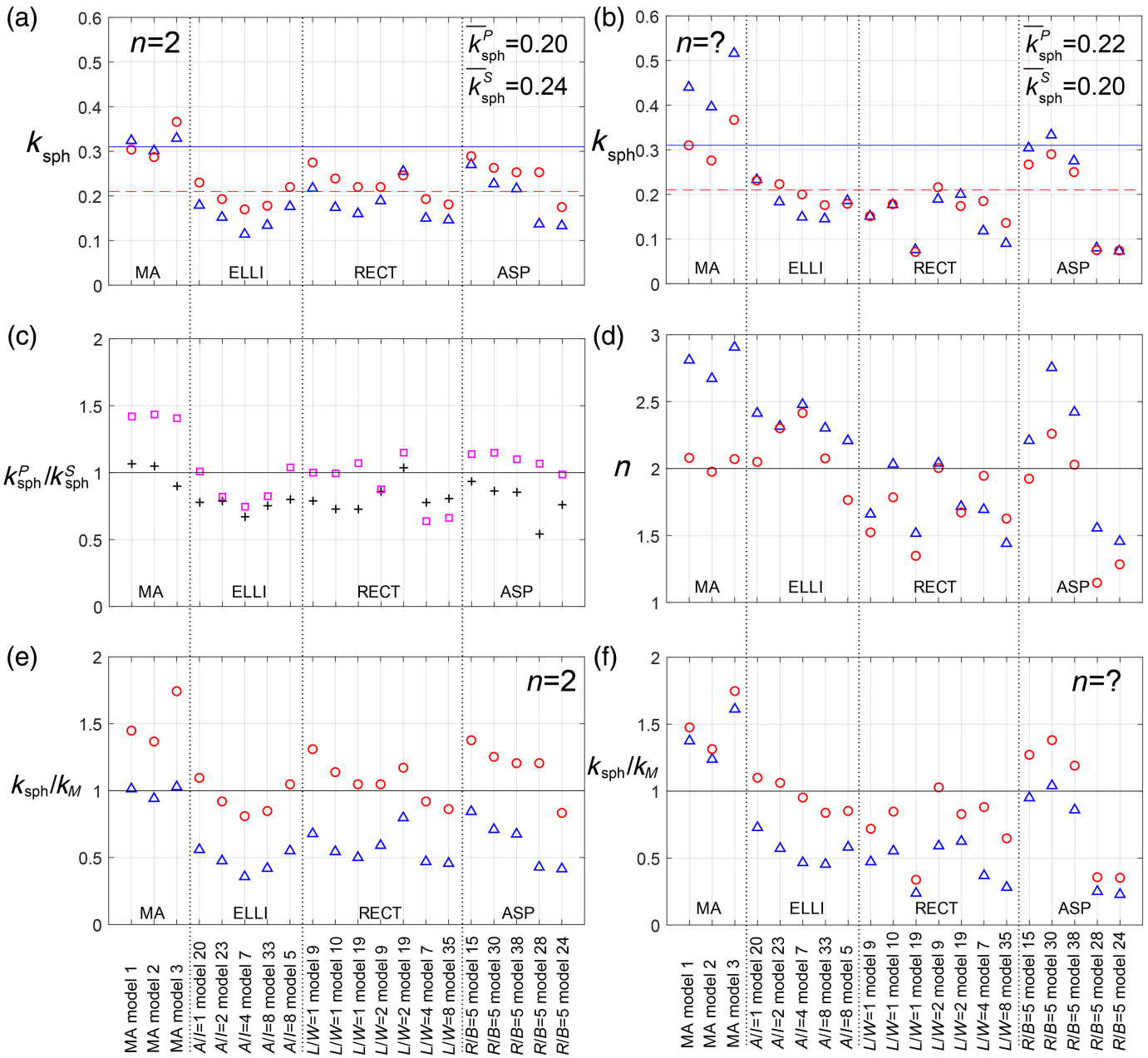

Figure 11. Average values of k over the focal sphere computed from our synthetic seismograms for (a) the spectral-fitting approaches with $n = 2$ and (b) the spectral fitting approaches with n fitted. Triangles and circles are the computed average k^P_{sph} and k^S_{sph} for the P and S waves, respectively. The solid and dashed lines given the values of k^P_M and k^P_M, respectively, from Madariaga (1976). (c) k^P_{sph}/k^S_{sph} for all models. The crosses and squares are k^P_{sph}/k^S_{sph} for $n = 2$ and n fitted, respectively. (d) The estimated n values from the spectral-fitting approach with n fitted. Triangles and circles are the computed average n^P and n^S for the P and S waves, respectively. The line indicates $n = 2$. Panels (e) and (f) demonstrate k_{sph}/k_M for $n = 2$ and n fitted, respectively. The color version of this figure is available only in the electronic edition.

family for most cases (Fig. 12), with the mean of the *bias* ranging from 0.08 to 0.58, corresponding to an overestimation of stress drop from 20% to 280%, on average. The MADs range from 0.03 to 0.24.

For the second-moment approach, most of the estimated values are tightly clustered around $\frac{\Delta\sigma_{est}}{\Delta\sigma_E} = 1.7$ for the MA model 1, corresponding to the *bias* mean of 0.22 (Figs. 12a, 13a). This means that the actual stress drop of 4 MPa is estimated as 6.8 MPa for most scenarios of the source depth and dip. We find that this is related to a slight underestimate of the source area (Fig. 15a). For the case with the largest depth and vertical fault, the second-moment approach underestimates the stress drop by a small factor (less than 2; Fig. 16a), which is related to poor azimuthal coverage by our station geometry.

For the spectral-fitting approach, using S waves with either $n = 2$ or n fitted, or P waves with n fitted, results in the mean overestimate by a factor of 2.5–3.5, with a spread between a factor of 1 and 10. This means that the actual stress drop of 4 MPa

TABLE 4
Averaged Source Parameters Computed Directly from the Spectral-Fitting Approach for a Focal Sphere; for Comparison, the Often-Used Values from Madariaga (1976) Are $k_M^P = 0.32$ and $k_M^P = 0.21$

		$n = 2$		$n = ?$			
Family (Set)	**Number**	k_{sph}^P	k_{sph}^S	k_{sph}^P	n^P	k_{sph}^S	n^S
MA model 1	1	0.32	0.30	0.44	2.81	0.31	2.08
MA model 2	1	0.30	0.29	0.40	2.67	0.28	1.98
MA model 3	1	0.33	0.37	0.52	2.91	0.37	2.07
ELLI (A/I = 1)	20	0.18	0.23	0.23	2.41	0.23	2.05
ELLI (A/I = 2)	23	0.15	0.19	0.18	2.31	0.22	2.30
ELLI (A/I = 4)	7	0.11	0.17	0.15	2.48	0.20	2.42
ELLI (A/I = 8)	33	0.13	0.18	0.15	2.30	0.18	2.08
ELLI (A/I = 8)	5	0.18	0.22	0.19	2.21	0.18	1.77
RECT (L/W = 1)	9	0.22	0.28	0.15	1.66	0.15	1.52
RECT (L/W = 1)	10	0.17	0.24	0.18	2.03	0.18	1.79
RECT (L/W = 1)	19	0.16	0.22	0.08	1.52	0.07	1.35
RECT (L/W = 2)	9	0.19	0.22	0.19	2.04	0.22	2.00
RECT (L/W = 2)	19	0.26	0.25	0.20	1.72	0.17	1.67
RECT (L/W = 4)	7	0.15	0.19	0.12	1.69	0.19	1.95
RECT (L/W = 8)	35	0.15	0.18	0.09	1.44	0.14	1.63
ASP (R/B = 5)	15	0.27	0.29	0.30	2.21	0.27	1.92
ASP (R/B = 5)	30	0.23	0.26	0.33	2.75	0.29	2.26
ASP (R/B = 5)	38	0.22	0.25	0.28	2.42	0.25	2.03
ASP (R/B = 5)	28	0.14	0.25	0.08	1.56	0.08	1.15
ASP (R/B = 5)	24	0.13	0.18	0.07	1.46	0.07	1.28

ASP, asperity-like; ELLI, elliptical; MA, Madariaga-like; RECT, rectangular.

is estimated as 10–15 MPa for most scenarios of the source depth and dip, with a spread between 4 and 40 MPa. Using P waves with $n = 2$ results in closer estimates, with the mean overestimate of only a factor of 1.2 and a smaller spread.

As already noted, we find that the differences between the actual and estimated stress drops for the spectral methods and MA sources are related to using incorrect values of k in formula (6), as already suggested for such sources by Kaneko and Shearer (2014) using average values of k for the entire focal sphere or sets of randomly chosen stations over the focal sphere. As often done for natural earthquakes, we obtain the spectral stress-drop estimates using the average values of k reported in Madariaga (1976). The values of k for our MA source MA model 1 are similar to those from Madariaga (1976) but not exactly the same (Figs. 9, 11). Both our MA sources and the sources in Madariaga (1976) are dynamically simulated aiming to reproduce a rupture starting at a point and spreading in all directions with a rupture speed of about 0.9β, but this is accomplished in slightly different ways, including the details of the nucleation procedure, the failure criterion (spontaneous rupture propagation with rate-and-state friction vs. imposed constant rupture speed with singular crack front), the slight variations and differences in the rupture speed (0.92β on average for MA model 1, Table 3 vs. imposed 0.9β), and the arrest procedure (a fault region of VS friction vs. unbreakable barrier). Even though ruptures in both our MA model 1 and in Madariaga (1976) spread nearly symmetrically away from a point resulting in a circular source with an average rupture speed of about 0.9β, the values of factor k (which relates the corner frequencies to the rupture duration) over the focal sphere are systematically larger for our MA model 1 (as well as MA models 2 and 3; Fig. 9a,b, Fig. S5). The averages are also not the same (Fig. 11), not only because the distributions of k are different but also because the averaging procedures are different (Text S1, Figs. S1, S2). Our averages are much closer to the values obtained by Kaneko and Shearer (2014) for their MA model which they call symmetrical circular rupture (Table 6).

Considering MA models with different abruptness of arrest, we find that the values of k indeed depend on the arrest, but in a relatively minor way compared to the effect of earthquake source asymmetry and shape discussed later for the other source families. For example, a change from the typical VS values we have used in prior modeling studies based on laboratory values (MA model 1) to much larger VS values (MA model 2; equivalent to the nearly unbreakable barrier used in Madariaga, 1976 and Kaneko and Shearer, 2014) results in relatively minor differences between the focal variations in k (Fig. 9a,b), with differences of average k values of only 10% or so (Fig. 11, Tables 4, 6). Even when one considers an almost velocity-neutral VS region (MA model 3), which is not an efficient barrier and results in significantly more gradual rupture arrest and wider moment-rate function (Fig. 2), the overall features of the focal distribution of k are similar (Fig. S5) and the average values of k

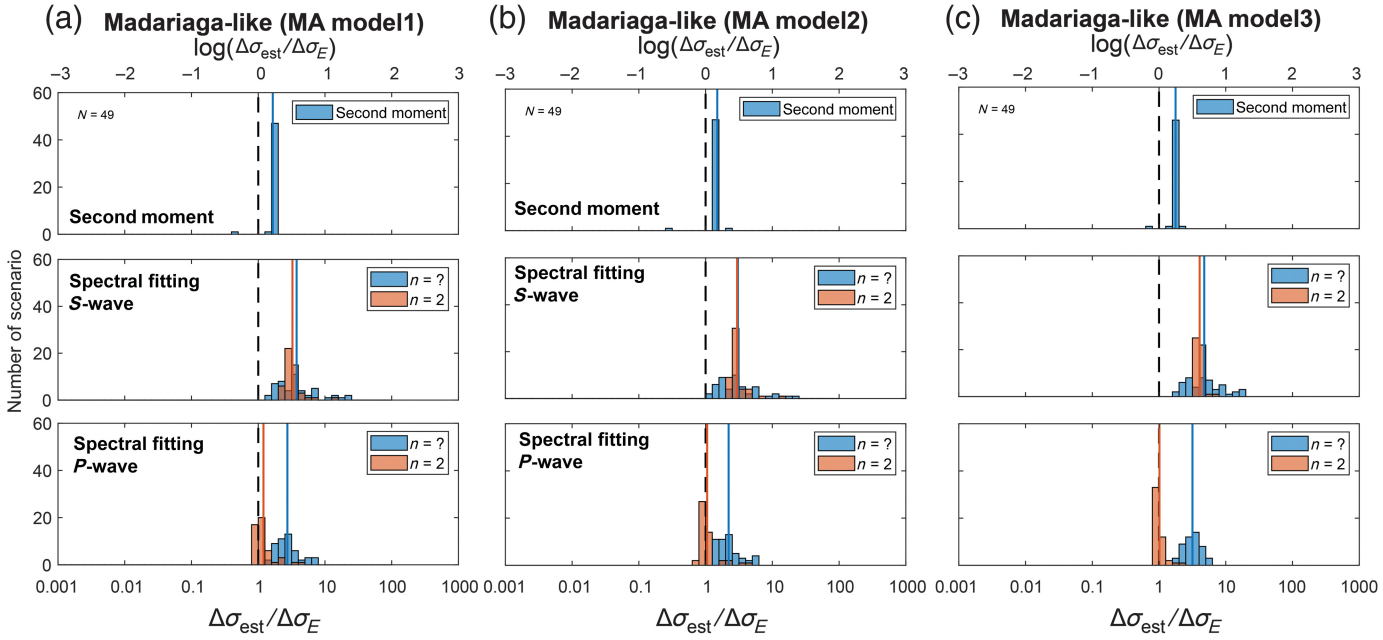

Figure 12. The ratio of the estimated to actual stress drops, ($\Delta\sigma_{est}/\Delta\sigma_E$), for all dip and depth scenarios (N = 49) and (a) MA model 1, (b) MA model 2, and (c) MA model 3. The results for the second-moment, spectral fitting (*S* wave), and spectral fitting (*P* wave) approaches are given in the top, middle, and bottom subfigures of each panel, respectively. The black-dashed lines indicate the ratio of 1. The blue- and orange-box plots are for the n fitted and n = 2 methods, respectively. The blue and orange lines show the corresponding mean stress-drop ratios.

increase by only about 30% (Table 6). This still makes a difference because the values of k enter the estimates of stress drops cubed (so a factor of 1.3 in k turns into a factor of 2.2 in stress drops), but this is a relatively minor effect compared to other source factors such as rupture directivity and source shape discussed later. Not surprisingly then, the comparison between the seismological estimates of stress drops and exact on-fault values is not much different between our three MA models with different arrests (Figs. 8, 12).

In addition to exploring different types of rupture arrest, another novel feature of our study of MA sources is that the stations cover only a specific part of the focal sphere determined by the depth and dip of the source, a practically important case. For the spectral-fitting approach, this introduces an additional source of difference in the appropriate value of k, as the relevant average of k would be the one over only the portion of the focal sphere represented by the stations. In other words, the ratio $\Delta\sigma_{est}/\Delta\sigma_E$ between the estimated and actual stress drops can be represented as follows:

$$\frac{\Delta\sigma_{est}}{\Delta\sigma_E} = \frac{7/16}{C_{act}}\left(\frac{k_{act}}{k_M}\right)^3 = \frac{7/16}{C_{act}}\left(\frac{k_{sph}}{k_M}\right)^3\left(\frac{k_{act}}{k_{sph}}\right)^3, \qquad (21)$$

in which k_{act} is the average of k values for the specific source of interest over the portion of the focal sphere populated by the stations, k_{sph} is the average of k values for the specific source of interest over the entire focal sphere, k_M is the average k values from Madariaga (1976), and C_{act} is the actual prefactor in the stress-drop expression (2). k_{act}, k_{sph}, and C_{act} depend on the actual earthquake source model, and k_{act} in addition depends on D/H and fault dip.

The effect of the partial compact coverage of the focal sphere by the receiver network for different fault depths and dips is shown in Figure 17a and Tables S2–S5. The cube of the ratio of the relevant k_{act} (average over the portion of the focal sphere represented by stations) and the spherically averaged k_{sph} for MA model 1 is shown for four methods (*P* and *S* waves with n = 2 and n fitted). The smallest effect is for the methods with n = 2, ranging from stress-drop overestimates by a factor of 2–5 for deep sources with zero dip, to minor stress-drop underestimates of 10%–25% for deep sources on a vertical fault (dip of 90°). The largest effect is for the *S*-wave method with n fitted, ranging from overestimates by a factor of up to 7 to underestimates by a factor of 2.

Although these values are consistent with the ones found in Kaneko and Shearer (2015) for an analysis with a random sampling of stations from the focal sphere, the novel finding here is that a compact array (as used in practice for local studies) introduces a systematic bias with depth even for MA sources in the case of a perfectly known path. For example, for a vertical fault and *P*-wave analysis with n = 2, the effect on the stress drop would range from an overestimate by a factor of 1.36 at the shallowest depths to a slight underestimate (factor of 0.88) for the deepest depths we consider. Put another way, an estimate of a constant stress drop with depth would actually mean that the stress drops systematically increase with depth by an overall factor of 1.5 for the range of depths we consider

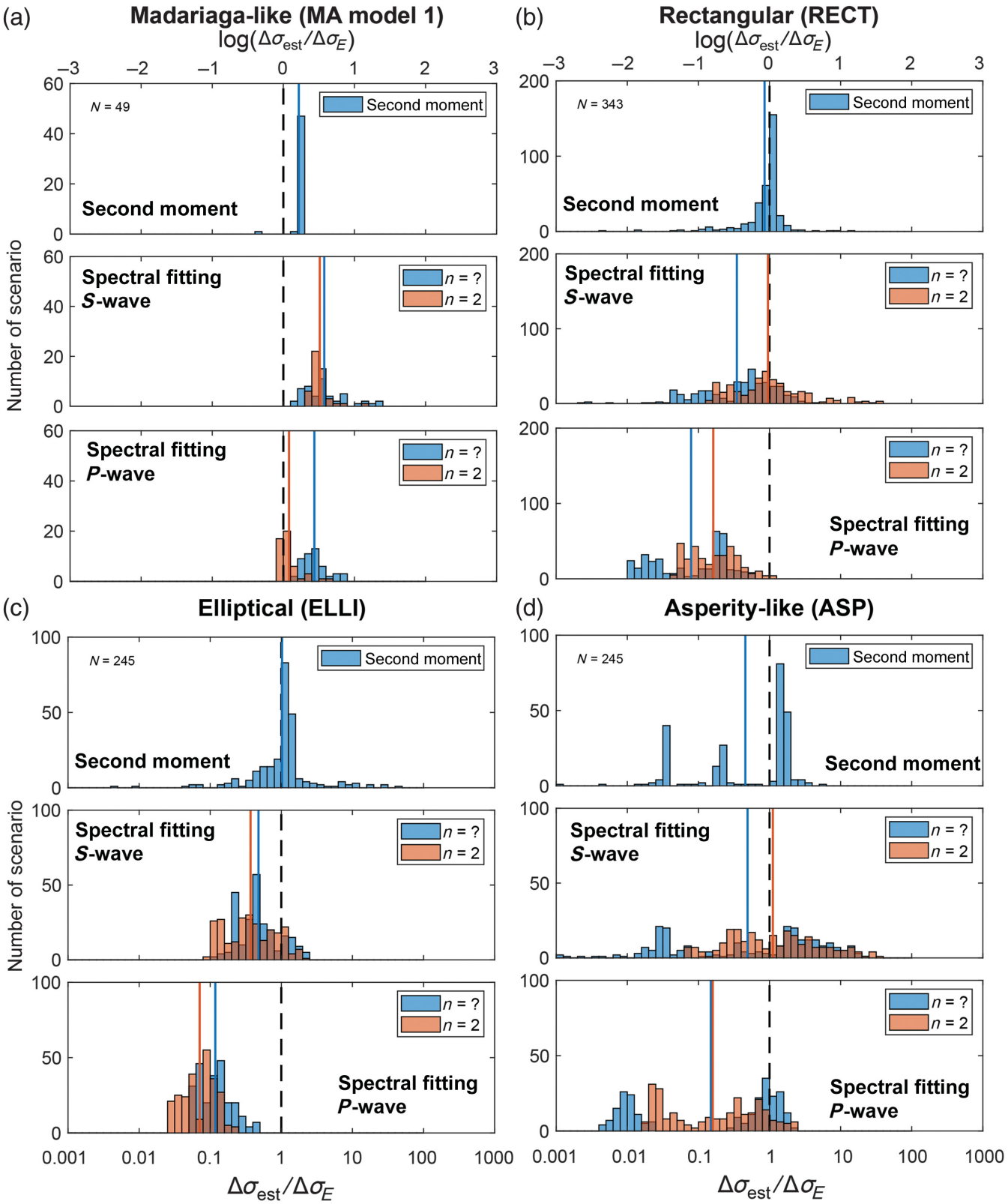

Figure 13. The ratio of the estimated to actual stress drops ($\Delta\sigma_{est}/\Delta\sigma_E$) for 49 dip and depth scenarios and earthquake sources from (a) the MA model 1, (b) the RECT family, (c) the ELLI family, and (d) the ASP family. The number of the resulting scenarios N is shown in each panel. The results for the second-moment, spectral fitting (S wave), and spectral fitting (P wave) approaches are given in the top, middle, and bottom subfigures of each panel, respectively. The black-dashed lines indicate a ratio of 1. The blue- and orange-box plots are for the n fitted and $n = 2$ approaches, respectively. The blue and orange lines show the corresponding mean stress-drop ratios.

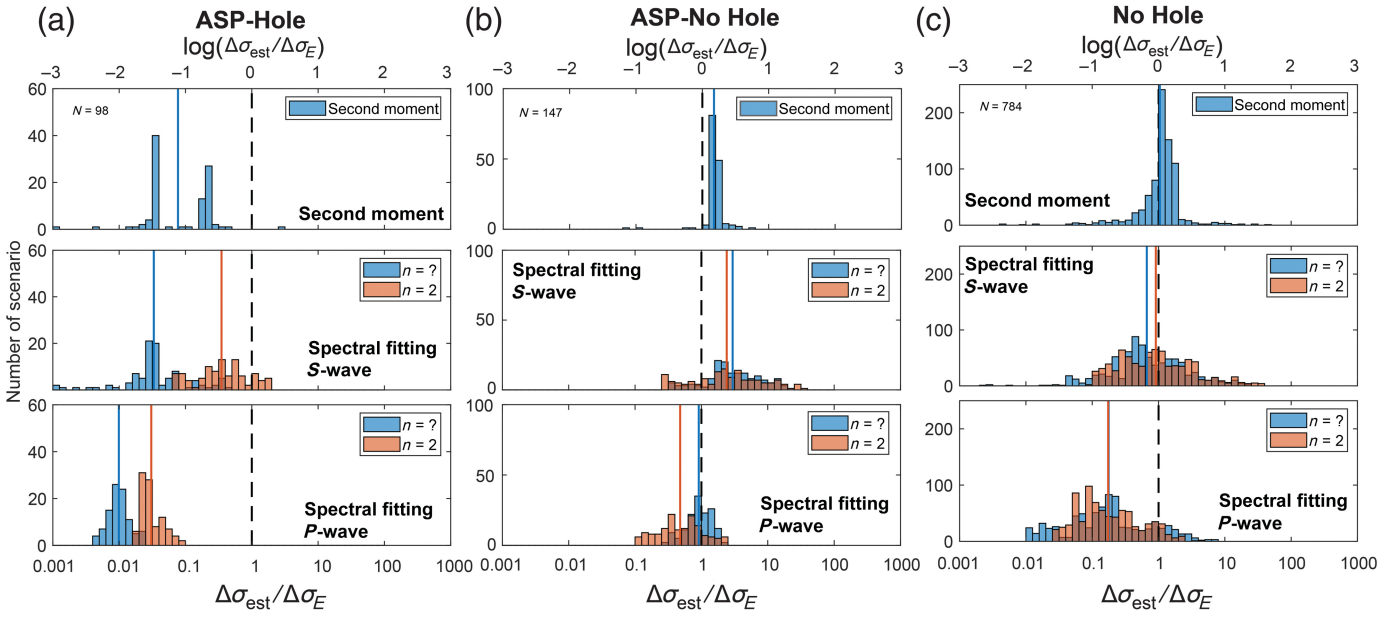

Figure 14. The stress-drop ratio ($\Delta\sigma_{est}/\Delta\sigma_E$) against a number of scenarios in (a) the ring-like models with a hole, (b) the models without a hole in the ASP family, and (c) the models without a hole in all families. Other plotting conventions are the same as in Figure 13.

here. This effect is even stronger for other types of sources as discussed in the following.

To demonstrate that the discrepancy in k is the main and only factor in the deviation of the estimated stress drops from the actual values for MA models (which are circular and axisymmetric), we plot both the ratio of the stress-drop estimate to the actual values (Fig. 16b, left panel) and the cube of the ratio between the actual values of k averaged over our stations to the values from Madariaga (1976) typically used in inversions (Fig. 16c, left panel), for different depths and dips of the MA source. The two are nearly identical (Fig. 16d, left panel). This means that the factor C_{act} in equation (21) is nearly 7/16 in this case, as we would expect for the symmetric circular rupture with nearly constant stress drop (e.g., Noda *et al.*, 2013).

We emphasize again that the discrepancy $\Delta\sigma_{est}/\Delta\sigma_E$ in the stress drops (Fig. 16b, left panel) and the values of k (Fig. 16c, left panel) combines (1) the discrepancy between the spherically averaged values of k_M from Madariaga (1976; Table 1) and spherically averaged values for k_{sph} for our MA model, MA model 1 (Tables 4, 6), which leads to overestimate of stress drops by a factor of $(0.30/0.21)^3 = 3.0$ and (2) the depth- and dip-dependent discrepancy between the averages over the appropriate part of the focal sphere and the average over the entire sphere given in Figure 17a, which ranges from overestimates by a factor of 2–5 for deep sources with zero dip to minor stress-drop underestimates of 10%–25% as already discussed. Hence the overall effect is the overestimate for all depths and dips with a systematic pattern. For example, for a vertical fault and *S*-wave analysis with $n = 2$ (Fig. 16b, left panel) of the MA model 1 event (with the actual stress drop of 4 MPa), the stress drop would be inferred as 4 times larger value (or 16 MPa) for the shallowest source we consider to 2.64 times larger value (or 10.6 MPa) for the deepest source we consider with a systematic variation in between.

Stress-drop estimates for the ELLI and RECT families

The second-moment approach performs well for the ELLI and RECT families, with the mean of *bias* being −0.07 and 0.01, respectively, corresponding to a slight underestimation and overestimation by factors of 15% and 2%, respectively (Fig. 13b,c, top panels). The MADs are 0.19 to 0.26 for both families, respectively. The results for one of the ELLI sources with $L/W = 4$ and different depths and dips (Fig. 16a, middle panel) indicate that the estimates are relatively accurate for most shallower depths and most dip angles; the deeper cases, especially on a vertical fault, have more discrepancy, up to a factor of 10. Examples of how the second-moment approach captures the area of the largest slip for these cases are shown in Fig. 15b,c. There is a systematic dependence of the stress-drop estimates with depth for some sources, such as the ELLI source ELLI $A/I = 4$ model 7 with horizontal directivity, especially for the vertical fault.

The mean of *bias* for the spectral fitting using the *S* wave is about −0.40 (except for the case of $n = 2$ in the RECT family where it is −0.02), indicating that the spectral fitting using the *S* wave underestimates stress drop by a factor of ∼2.5 on average (Fig. 13b,c, middle panels). The MADs for the ELLI family range from 0.24 to 0.29 and for the RECT from 0.38 to 0.45. The mean of *bias* for the spectral-fitting approach using the *P* wave is about −1.0 in the RECT and ELLI families, which means that the stress drops are underestimated by a factor of ∼10 on average (Fig. 13b,c, bottom panels). The MADs for the ELLI family range from 0.19 to 0.20, which are smaller than those for the RECT, ranging from 0.29 to 0.48.

TABLE 5
Determined Statistic Parameters for the Conditions in the Present Study

		The Spectral-Fitting Approach (*P* Wave)						The Spectral-Fitting Approach (*S* Wave)						The Second-Moment Approach		
		n= ?			*n* = 2			*n*= ?			*n* = 2					
Condition	***N***	$\Delta\sigma_{est}/\Delta\sigma_E$	***bias*** **mean**	***bias*** **MAD**	$\Delta\sigma_{est}/\Delta\sigma_E$	***bias*** **mean**	***bias*** **MAD**	$\Delta\sigma_{est}/\Delta\sigma_E$	***bias*** **mean**	***bias*** **MAD**	$\Delta\sigma_{est}/\Delta\sigma_E$	***bias*** **mean**	***bias*** **MAD**	$\Delta\sigma_{est}/\Delta\sigma_E$	***bias*** **mean**	***bias*** **MAD**
MA model 1	49	2.733	0.44	0.13	1.199	0.08	0.10	3.758	0.58	0.24	3.255	0.51	0.08	1.653	0.22	0.03
RECT	343	0.079	–1.10	0.48	0.162	–0.79	0.29	0.348	–0.46	0.45	0.951	–0.02	0.38	0.853	–0.07	0.19
ELLI	245	0.118	–0.93	0.19	0.071	–1.15	0.20	0.477	–0.32	0.24	0.369	–0.43	0.29	1.026	0.01	0.26
ASP	245	0.149	–0.83	0.94	0.159	–0.80	0.58	0.491	–0.31	0.94	1.113	0.05	0.53	0.457	–0.34	0.64
ASP-Hole	98	0.010	–2.01	0.12	0.031	–1.52	0.13	0.033	–1.48	0.37	0.349	–0.46	0.32	0.077	–1.11	0.45
ASP-Nohole	147	0.912	–0.04	0.15	0.479	–0.32	0.28	2.951	0.47	0.32	2.399	0.38	0.44	1.514	0.18	0.08
Nohole	784	0.177	–0.75	0.49	0.174	–0.76	0.39	0.665	–0.18	0.46	0.910	–0.04	0.45	1.047	0.02	0.21
Nohole (eight stations)	784	0.174	–0.76	0.49	0.170	–0.77	0.40	0.646	–0.19	0.47	0.891	–0.05	0.46	1.097	0.04	0.37

ASP, asperity-like; ELLI, elliptical; MA, Madariaga-like; MAD, median absolute deviation; and RECT, rectangular.

The main reason for these significant average underestimates by the spectral approaches is increasingly different distributions of k over the focal sphere for sources from the ELLI and RECT families from the distributions of k for the MA models. Physically, this is due to their tendency for asymmetry (unidirectional propagation) and their deviation from the spherical shape. As identified by Kaneko and Shearer (2015), an asymmetric circular source (exemplified by our ELLI A/I = 1 model 20) already leads to substantial differences in the distribution of k (Fig. 9c), with the focal-sphere averages for the case of n fitted differing from Madariaga (1976) values by a factor of 0.23/0.32 = 0.72 and 0.23/0.21 = 1.09 for the P and S waves, respectively (Tables 4, 6). This translates into stress-drop underestimates with factor of $0.72^3 = 0.37$ (about three times smaller) and overestimate with a factor of $1.09^3 = 1.3$ for the P and S waves, respectively. The difference is even larger for the P-wave case with n = 2. As also shown by Kaneko and Shearer (2015), the differences with MA models are further amplified for asymmetric ELLI sources of aspect ratio 2 (exemplified by our ELLI A/I = 2 model 23), with the distribution of k over the focal sphere (Fig. 10a) leading to even lower spherically averaged values (Tables 4, 6) which translate into stress-drop underestimates with factors $(0.18/0.32)^3 = 0.15$ (about eight times smaller) and stress-drop overestimates with factors $(0.22/0.21)^3 = 1.15$ (about 15% larger) for the P and S waves, respectively, with the n-fitted approach.

We show that asymmetric ELLI sources with higher aspect ratios of 4 and 8 amplify this trend further (Fig. 10c, Fig. S6), with even lower values of average k and an even larger impact on stress-drop estimates. We also note that the shape of the distribution of k over the focal sphere is similar for asymmetrical sources which are circular and ELLI (Figs. 9c, 10), with most of the values becoming lower for the higher aspect ratios of the source, and different from that for the MA source (Fig. 9a,b and Fig. S5).

Further, we find a strong systematic effect of the depth of the source on spectral estimates of stress drops for these asymmetric and/or higher-aspect-ratio sources, given a compact network array. An example for ELLI A/I = 4 model 7 with actual stress drop of 3 MPa and S-wave spectral fitting with n = 2 (Fig. 16b, middle panel) shows the strong systematic effect of depth, from mild overestimate for the shallowest case (estimated stress drop is larger by a factor of 1.1 resulting in 3.3 MPa) to a significant underestimate for the deeper cases (up to 10 times smaller, resulting in stress-drop estimates of 0.3 MPa at depth). This is despite the fact that the average value of k over the focal sphere is not very different for this specific case from the Madariaga value, 0.17 versus 0.21, with a ratio of 0.8, the cube of which is only 0.5 (which would lead to twice smaller stress-drop underestimates). So most of the disparity in stress-drop estimates for this case is actually due to significant differences between the values of k averaged over the entire focal sphere, k_{sph} versus the appropriate average k_{act} over only

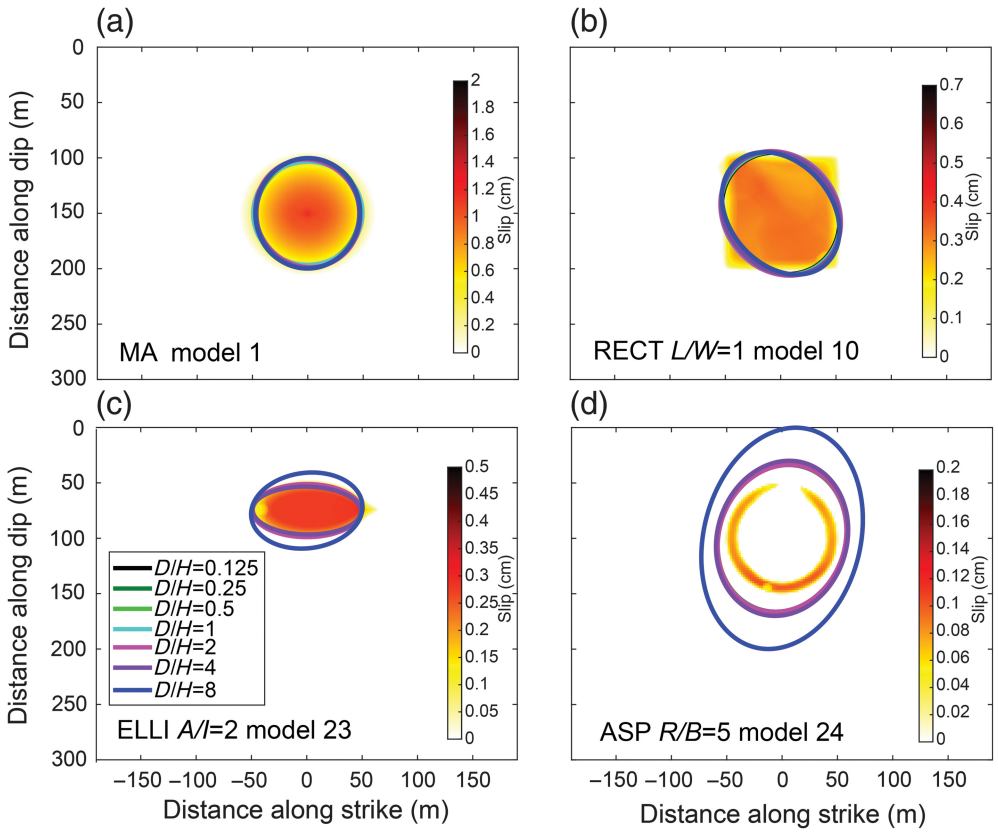

Figure 15. Comparisons of the actual rupture areas and the areas determined from the second-moment approach for: (a) MA model 1, (b) RECT $L/W = 1$ model 10, (c) ELLI $A/I = 2$ model 23, and (d) ASP $R/B = 5$ model 24. For each panel, seven cases are plotted for different depths of the source, all with the dip = 60°, indicated by ellipses of different colors. The colored area in the background is the final slip (in centimeters) from the dynamic models. The color scale for slip is shown on the right of each panel.

a portion of it that corresponds to the station locations. As shown in Figure 17b and Tables S6–S9, this results in a systematic effect with depth, with stress-drop overestimated by a factor of 2 to 2.5 for the shallowest depth to stress-drop underestimated by a factor of 0.2 (five times smaller) at depth. This depth-dependent stress drop bias is much larger than the factor of 0.5 due to the difference in the spherically averaged value of k between this source and the one from Madariaga (1976). We note that this significant depth-dependent disparity cannot be corrected by using Madariaga (1976) model and taking averages over the appropriate portions on the focal sphere. This is because the focal distribution of k is very different for asymmetrical ELLI sources (including example one, ELLI $A/I = 4$ models 7, Fig. 10b) and for MA symmetrical circular models (Fig. 9a,b). A similar but more mild artificial depth-dependent trend also exists for the second-moment estimates for this source (Fig. 16a, middle panel).

There is virtually no dip dependence of the spectral stress-drop estimates for ELLI $A/I = 4$ model 7 (Fig. 16b, middle panel). This is because the source directivity is horizontal and the ELLI source is rather narrow, and hence the source is close to a horizontal line source, something that would not be much affected by a change in dip. Indeed, considering precise averages over the relevant portions of the focal sphere (Table S8), we see that there are some variations with dip but they are very minor.

To show that the combined difference in k (dominated by the depth-dependent differences due to the observational array as just discussed) accounts for most of the discrepancy between actual and estimated stress drops, we plot, for the same ELLI source as an example, both the ratio of the stress-drop estimates to the actual values (Fig. 16b, middle) and the cube of the ratio between the actual values of k averaged over our stations for the appropriate angles and the average value from Madariaga (1976) typically used in inversions (Fig. 16c, middle) for different depths and dips. We see that the plots are very similar. The ratio of the values of the two panels varies between 1.12 and 2.72, indicating that there is another, more minor, reason for the discrepancy. From the structure of expression (21), it corresponds to the prefactor C_{act} that should have been used instead of 7/16 due to the noncircular shape of the source and the fact that we are trying to match the (slightly larger) energy-based stress drop. However, these effects are relatively insignificant for these families compared to the effect of the discrepancy in the values of k.

The sources from the RECT family with the aspect ratio of 2 and larger result in more or less unidirectional horizontal propagation from one edge of the fault to the other (RECT $L/W = 2$ model 9, RECT $L/W = 4$ model 7, RECT $L/W = 8$ model 35 in Fig. 4) and produce results similar to the unidirectional (asymmetrical) sources from the ELLI family. The shape of the k distributions and trend of the decrease in many values of k for larger aspect ratios are similar to those for the ELLI asymmetric sources (Figs. S6, S7). In the three RECT models with the square fault geometry ($L/W = 1$), the rupture mostly spreads from one corner to the opposite one, broadly similar to the asymmetric circular model (ELLI $A/I = 1$ model 20), but these models have a varying degree of additional complexity in terms of varying directions of slip (Fig. 4), which results in different distributions of k over the focal sphere

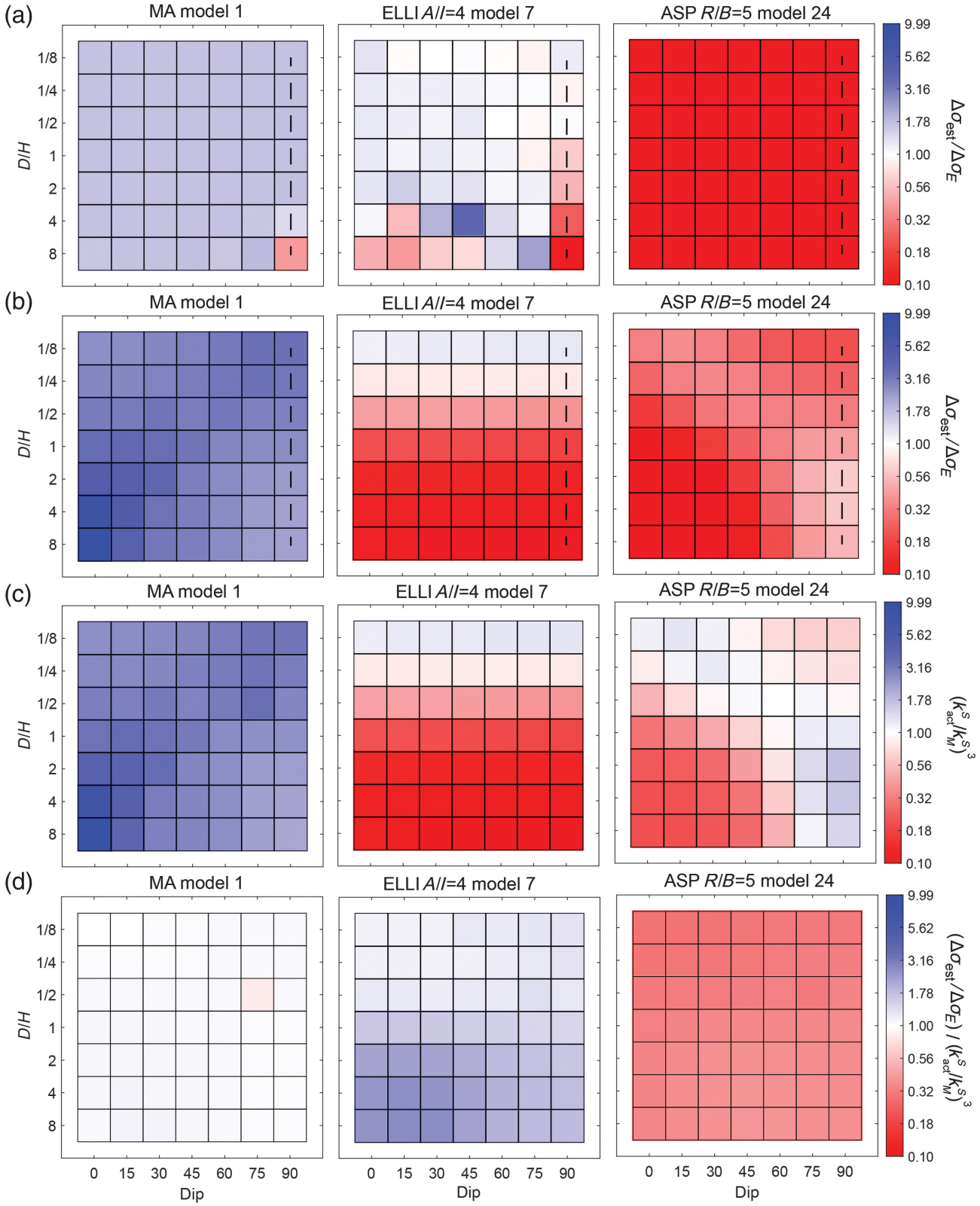

Figure 16. Examples of results for different source dip and normalized depth D/H (the ratio of the depth to the half-width of the station network) for three sources: MA model 1 (left column), ELLI $A/I = 4$ model 7 (middle column), and the ASP $R/B = 5$ model 24 (right column). (a) The estimated stress drop ratio $(\Delta\sigma_{est}/\Delta\sigma_E)$ for the second-moment approach, (b) the estimated stress-drop ratio $(\Delta\sigma_{est}/\Delta\sigma_E)$ for the spectral-fitting approach (S wave, $n = 2$), (c) $(k^S_{act}/k^S_M)^3$, in which the k^S_{act} is the average value computed over the focal-sphere portion covered by the network using the actual values of k for the particular source model and k^S_M is the value from Madariaga (1976), and (d) ratio of values in panels (b) and (c), $(\Delta\sigma_{est}/\Delta\sigma_E)/(k^S_{act}/k^S_{Mad})^3$ that quantify any residual mismatch. In panels (a,b), the blue and red colors correspond to the overestimated and underestimated values, respectively. Note that the cases for $D/H \le 0.5$ are appropriate for crustal earthquakes (focal depth ≤ 21.2 km).

TABLE 6
Comparison of Estimated k and n for Similar Models in Kaneko and Shearer (2014, 2015) and the Present Study

Compared Models	v_R/β	k^P_{sph}	k^S_{sph}	k^P_{sph}/k^S_{sph}	n^P	n^S
Symmetrical circular*	0.90	0.38	0.26	1.46	2.4*	1.9*
MA model 1	0.92	0.44	0.31	1.42	2.81	2.08
MA model 2	0.93	0.40	0.28	1.43	2.67	1.98
MA model 3	0.89	0.52	0.37	1.41	2.91	2.07
Asymmetrical circular*	0.80	0.27	0.26	1.04	2.2*	2.1*
ELLI A/I = 1 model 20	0.77	0.23	0.23	1.00	2.41	2.05
Asymmetrical elliptical*	0.90	0.25	0.26	0.96	2.2*	2.2*
Asymmetrical elliptical*	0.70	0.19	0.19	1.00	–	–
ELLI A/I = 2 model 23	0.82	0.18	0.22	0.82	2.32	2.30

ELLI, elliptical; MA, Madariaga-like.
*Models proposed in Kaneko and Shearer (2015); the values of n in that work are given with one significant decimal digit.

(Figs. S8, S9) and larger spread of stress-drops estimates (Fig. 8) compared to the asymmetric circular model (ELLI A/I = 1 model 20).

Stress-drop estimates for the ASP family

For the sources in the ASP family, the *bias* from the second-moment approach has three peaks at −1.5, −0.7, and 0.2 (Fig. 13d, top panel). The reason for these peaks becomes clear when we plot separately the results for the sources that rupture the entire seismogenic patch ("ASP-No hole," Fig. 14b) and those that rupture only the circumference of the ASP model ("ASP-hole," Fig. 14a). Results for the sources without the hole are similar to those for the Madariaga family (with the same mean *bias* but more spread for the ASP sources) resulting in the overestimate of the stress drop by a factor of ∼1.7. For the sources with the hole, there are two *bias* peaks at −1.5 and −0.7, corresponding to the stress-drop underestimate by a factor of 32 and 5, respectively. Clearly, the second-moment approach overestimates the rupture area in these cases because it represents the partial ring-like rupture of the seismogenic region by a compact larger ellipse which varies with depth due to changes in station coverage, as illustrated in Figure 15d for one of the ASP sources.

For the spectral-fitting approach, the results using S waves (Fig. 13d, middle panel) have a mean *bias* closer to zero (even as small as −0.05 for n = 2 case) than those using P wave (Fig. 13d, bottom panel). The MADs for the spectral approaches are similar, around 0.55, and smaller than the one for the second-moment approach. However, the distribution is relatively flat, indicating that only a relatively small fraction of sources have a small bias. Indeed, by considering separately cases without and with a hole (Fig. 14a,b), we see that the mean *bias* for the cases without a hole is similar to the case of MA source but with a larger spread in values; in particular, it is 0.5 when using S waves and n = 2 (and no longer equal to zero); this is balanced by the underestimate for the cases with the hole. All spectral methods significantly underestimate stress drops for cases with the hole, by more than a factor of 10 on average (*bias* mean < −1), except the spectral-fitting approach (S wave, n = 2), which underestimates by a factor of 3 on average (*bias* mean = −0.46). The spectral-fitting approach of S waves with n = 2 performs better than any other method, including the second-moment approach.

To understand the discrepancies for the sources from the ASP family when using spectral approaches, we again consider the values of k for such sources (Fig. 10c, Fig. S10, S11). The distributions and average values of k for the cases in which the whole asperity is ruptured (Fig. S10) are more or less in between those for the MA source (MA model 1) and the asymmetrical circular source (ELLI A/I = 1 model 20; Fig. 9), which explains the performance of spectral methods for these sources close to the MA models but with a larger spread. When the whole asperity is ruptured in the ASP family, the source typically contains multiple slip directions (Fig. 5), which is a feature similar to the MA source in which slip spreads in all directions on the fault. However, the distributions and average values of k are substantially different—mostly substantially smaller—for the ring-like sources (Fig. 10c, Fig. S11).

The estimated stress drops again strongly depend on the dip and depth of the sources, as illustrated for one of the ring-like sources (ASP R/B = 5 model 24) in Figure 16b (right panel). In contrast to the ELLI A/I = 4 model 7 (Fig. 16b, middle panel), the dependence is no longer mainly with depth. The pattern is similar to the MA model (Fig. 16b, left panel), but with the underestimate of stress rather than overestimate. There is again a systematic dependence with depth, but the underestimate increases with depth for some dips (0°–45°) and decreases for others (90°, which corresponds to a vertical fault). Because this spectral approach (S waves, n = 2) performs best for ring-like sources, the underestimate of the stress drops would be much larger (by an additional order of magnitude or so) for the other spectral approaches.

The cube of the ratio of the actual average k_{act} (computed for this source and over only the relevant part of the focal sphere) and the average value k_M from Madariaga (1976; Fig. 16c, right panel) has similar pattern with different dips

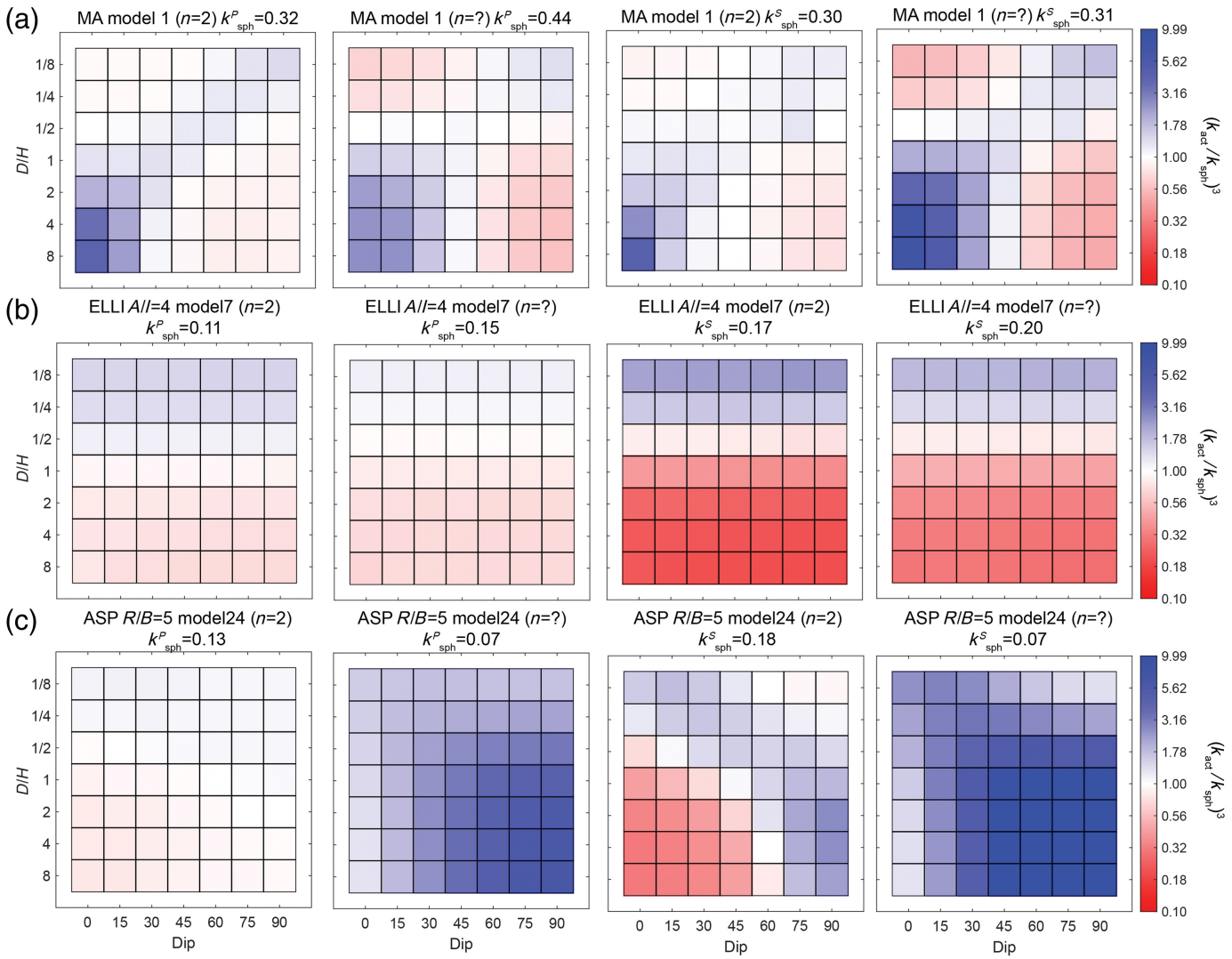

Figure 17. The effect of using a compact station network (Fig. 6) on stress-drop estimates for the three earthquake sources of Figure 16, quantified through the ratio $(k^S_{act}/k^S_{sph})^3$, in which the k^S_{act} is the average value computed over the focal-sphere portion covered by the network and k^S_{sph} is the average value over the entire focal sphere, using the actual values of k for the particular source model in both. Note that the cases for $D/H \leq 0.5$ are appropriate for crustal earthquakes (focal depth $\leq$ 21.2 km).

and depths, showing that the difference in k again significantly contributes to the pattern of underestimated stress drops. However, the two plots have somewhat different values. Looking at the ratio of Figure 16b,c panels for this case (Fig. 16d, right panel), we find that this discrepancy is nearly constant, with a factor of 0.29–0.4. From the structure of stress-drop expression (21), it clearly corresponds to the prefactor C_{act} that should have been used instead of 7/16 due to the ring-like shape of the source and the fact that we are trying to match the (larger) energy-based stress drop.

One approximate way to easily understand the basis for significant average underestimate of stress drops for asymmetric elongated sources (ELLI and RECT, aspect ratio of 2 or higher) and ring-like sources from the ASP family is to consider the difference in the source area between them and the symmetric circular MA model of the same rupture speed and duration, as done in the study of Lin and Lapusta (2018). Spectral approaches essentially try to determine the rupture duration from the average corner frequency, and then assume, if MA models are envisioned, that the rupture is a filled circle with the radius given by the rupture duration times a fraction of the shear-wave speed. However, the actual source area can be much smaller, for example, a (slim) torus for the ring-like models, or an elongated ellipse with unidirectioinal propagation. Using a (much) larger area in formula (6) for the stress drop would lead to a (significant) underestimate of the stress drop. Mathematically, this manifests itself in the discrepancy in spherically averaged k as already discussed. This overall underestimate is then modulated by various methods of estimating the corner frequency (S vs. P wave, n = 2 vs. n fitted, various fitting procedures, etc.), the differences in the rupture duration obtained by considering only a portion of the focal sphere that corresponds to the available stations, and by the prefactor in the stress-drop expression (6), which is different for different

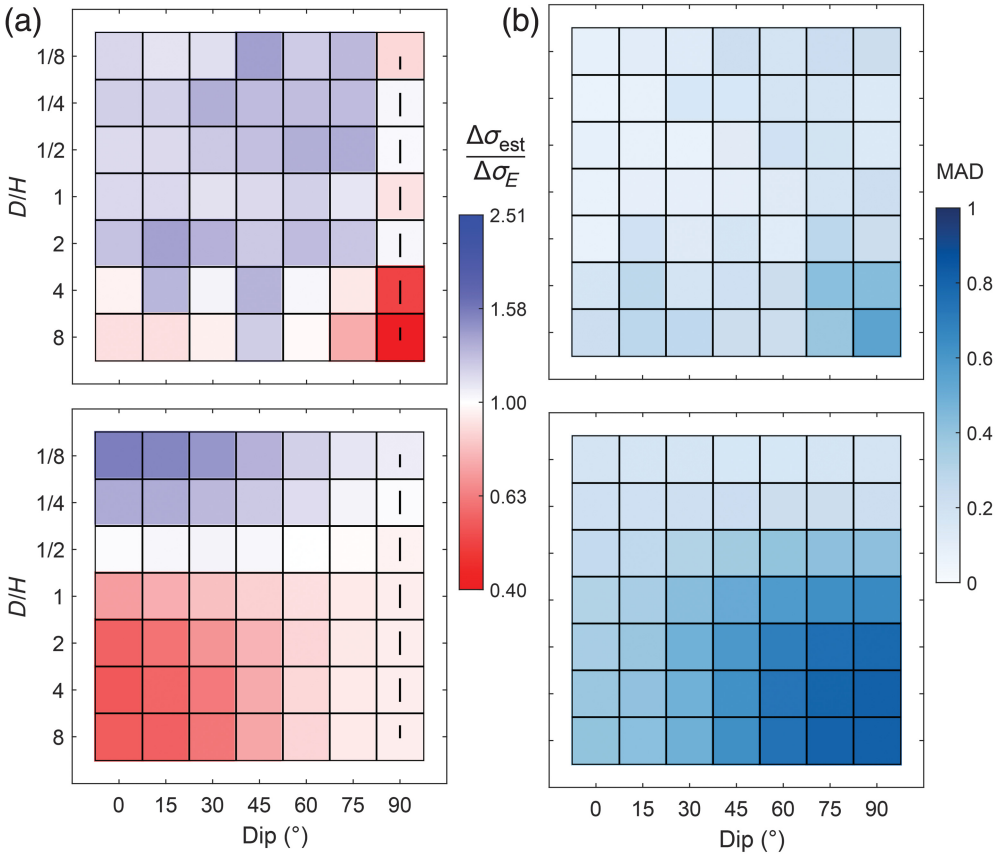

Figure 18. (a) The averages of the ratio of the estimated to actual stress drops ($\Delta\sigma_{est}/\Delta\sigma_E$) for all source models for different source depths and dips using (top) the second-moment approach and (bottom) the spectral-fitting approach (*S* wave, $n = 2$). The blue and red colors correspond to overestimated and underestimated stress drops, respectively. The vertical-dashed line indicates $\Delta\sigma_{est}/\Delta\sigma_E$ for a vertical fault. (b) The scattering of the stress-drop ratio for the same cases is measured by median absolute deviation (MAD). Darker colors correspond to larger scattering in stress-drop estimates. Note that the cases for $D/H \leq 0.5$ are appropriate for crustal earthquakes (focal depth ≤ 21.2 km).

source shapes. Additional discussion about the ring-like sources can be found in Lin and Lapusta (2018).

Dependence on focal depth and fault-dip angle

Let us consider $\frac{\Delta\sigma_{est}}{\Delta\sigma_E}$ for each considered composition of focal depths and fault dips for all earthquake source scenarios (Fig. 18). Here, we only focus on the results from two approaches that perform best overall, the second-moment approach and the spectral-fitting approach based on *S* waves with $n = 2$. The second-moment approach tends to overestimate the stress drops for most depths and dips, other than the deepest locations and for the vertical fault. The second-moment approach performs poorly for large depths (more than 160 km) on vertical faults, which is understandable because it is difficult to determine differences in apparent source duration on the limited-extent array on the surface if an earthquake occurs on a vertical fault. The spectral-fitting approach using *S* waves with $n = 2$ results in a systematic depth dependence of the estimated stress drops. Such a systematic depth dependence of the stress-drop estimates strongly depends on the features of the earthquake source and occurs also for the second moment for some earthquake sources (Fig. 15).

DISCUSSION AND CONCLUSIONS

Second-moment approach: good performance for compact sources, poor for ring-like ruptures

Our results show that, in the absence of path and site effects and with relatively dense station coverage of zero noise, the second-moment approach performs well overall for estimating the stress drop of compact sources (ruptures with no holes) for which it is highly suitable, as also clear from past studies (Backus and Mulcahy, 1976; Backus, 1977; Silver, 1983; Silver and Jordan, 1983; McGuire *et al.*, 2001, 2002, McGuire, 2004, 2017; Fan and McGuire, 2018; McGuire and Kaneko, 2018). This method estimates stress drop relatively accurately (only 4% overestimation on average). Most of stress-drop estimates range from 66% to 150% of the true values (Fig. 14c). Larger deviations arise for deeper sources due to limited station coverage assumed in this study. However, the second-moment approach has poor performance, with a mean factor of 10 underestimation, for ring-like sources with a hole (Fig. 14a), which results from significant overestimation of rupture area because the second moment interprets such sources as filled. For such sources, its performance is not as good as the spectral fitting of *S* waves with $n = 2$, but comparable to the spectral methods overall.

Spectral approaches: larger scatter overall, better performance for ring-like ruptures

Out of the spectral-fitting approaches, the one based on *S* waves with $n = 2$ performs the best overall for the earthquake sources and network-depth-dip configurations considered in this work. It works well for the RECT and ASP families with approximately zero mean *bias*. Although it overestimates stress drops by a factor of ~3 on average for our MA source, and underestimates by

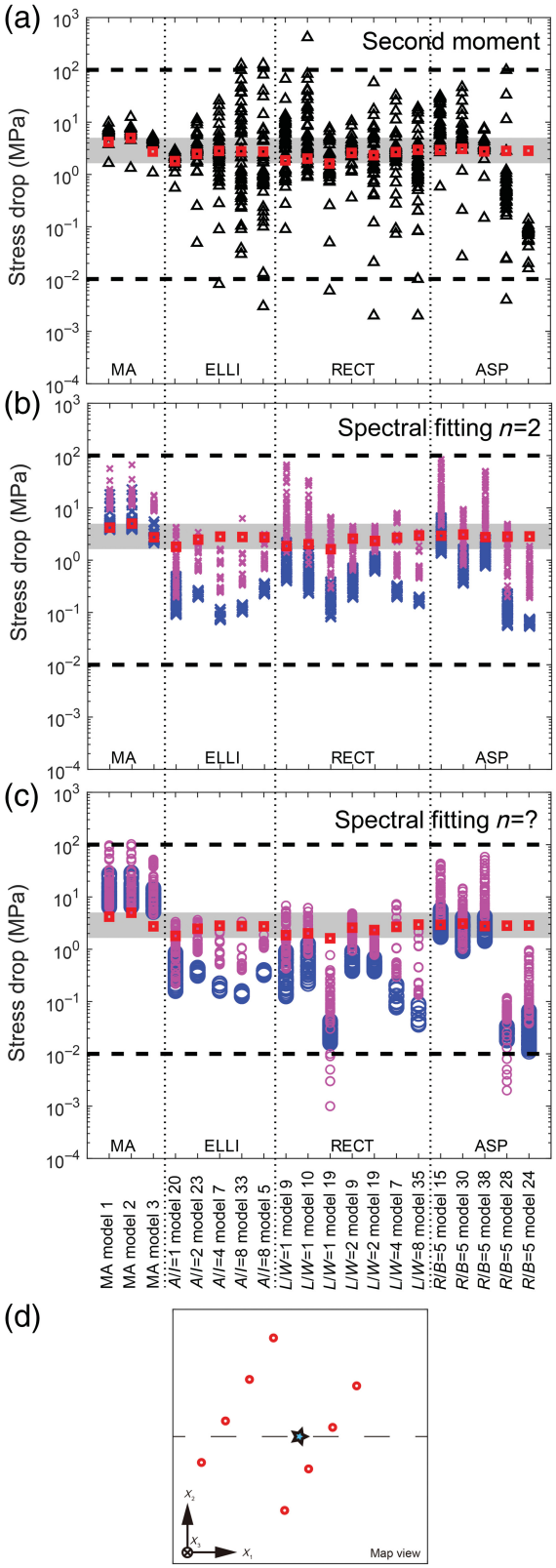

Figure 19. Seismologically estimated stress drops ($\Delta\sigma_{est}$) for all models using eight stations and (a) the second-moment approach, (b) the spectral-fitting approach ($n = 2$), and (c) the spectral-fitting approach (n fitted). The plotting conventions are the same as in Figure 8. (d) Distribution of the eight pseudostations.

a factor of ~3 on average for the ELLI sources, it then has near zero mean *bias* for the sources without a hole overall. For ring-like sources with a hole, it has a smaller average underestimate than the other methods. The spectral-fitting approach based on *S* waves with $n = 2$ has larger scattering than that from the second-moment approach. Most of the stress-drop estimates range from 33% to 300% of the true value, with the spread overall being about 0.01–100 MPa. Our results show that the spectral-fitting approaches based on *P* waves with $n = 2$ is the best one for MA sources, but for other types of sources it produces larger deviations, mainly significant underestimates, than the approach based on *S* waves. This is because the spherical averages of k values for our sources are closer overall to Madariaga values for *S* waves than for *P* waves (Fig. 11e,f). Somewhat surprisingly, the spectral approaches based on fitting n produce larger deviations than the ones with $n = 2$, something that we plan to investigate in detail in the future.

Significantly different distributions of corner frequencies for our sources and systematic effects of network geometry

There are three main reasons for the discrepancy between the actual stress drops and their estimates by the spectral methods (equation 21), when the path effects are known and site effects are nonexistent, as in our study.

The first main reason is using predetermined average k values for specific simple sources, such as for the circular source from Madariaga (1976), as pointed out by Kaneko and Shearer (2014, 2015) for asymmetric circular, symmetric elliptical, and asymmetric elliptical sources of aspect ratio 2. The k values map the estimated corner frequencies into estimated rupture dimensions and enter the stress-drop expression cubed. In our earthquake source models that use lab-derived rate-and-state friction laws, one has to make special assumptions to create MA sources, enforcing nucleation in the middle of a (otherwise homogeneous) patch by prescribing higher shear stress there and adjusting prestress over the patch to result in near-constant rupture speeds. Yet, our basic MA source, MA model 1, while very similar in terms of geometry and rupture speed to those in Madariaga (1976), has slightly different initiation, failure law, and arrest, and already results in larger average k for *S* waves by the factor of about 1.5 compared with Madariaga (1976; Table 4) and hence larger estimate of stress drops by the average factor of $(1.5)^3 = 3.4$. We note that our average k values are close to the ones obtained in Kaneko and Shearer (2015) for similar sources (Table 6). The differences in average values of k significantly amplify for the dynamic sources of different shapes and directivity (Table 4, Fig. 11). As noted by Kaneko and Shearer (2015), just considering an asymmetric circular source or a narrower elliptical source of aspect ratio 2 already produces a noticeable decrease in the average values of k. We show that this trend continues for slimmer asymmetric sources, such as ELLI and RECT sources of higher aspect ratios.

Additional source complexities, such as variable slip directions in RECT and ASP families, further complexify this picture, with the average values of k actually increasing for some of such sources. Ring-like sources can have average k values as small as 0.07–0.08 for n-fitted method. The decrease in k for many sources considered in this study leads to significant overall underestimate of the stress drops, especially for the asymmetric ELLI and RECT sources and ring-like sources. If such sources are typical on natural faults, then the mean stress drops for small events may be underestimated.

The second main reason is the station geometry in relation to the source depth and dip, which creates systematic significant changes in the stress-drop estimates. This is because the relevant average for k is over the angles corresponding to the station locations and not the entire focal sphere. The station geometry effect can rival in magnitude the effect of the average discrepancy in the values of k, adds significantly to the scatter of stress drops, and strongly depends on the shape and directivity of the source. The contribution of the incomplete random coverage of the focal sphere by stations has already been pointed out by Kaneko and Shearer (2015); the novel finding here is that compact station geometry, as often used in practice, can introduce significant systematic bias with depth discussed more in the following. Because the distribution of k values over the focal sphere is quite different for the MA sources and the other sources we consider, one cannot use partial averages of k for the MA sources to correct for this issue; indeed, the averages of k over the portions of the focal sphere populated by the station network significantly differ for different sources we consider (Fig. 17, Tables S2–S13).

The third reason for the discrepancy between the actual and spectrally estimated stress drops is the use of formulas based on the circular source. Specifically, the prefactors in formulas (3) and (6) for the stress drop are for the circular sources of uniform stress drop and would be different for different source shapes or nonuniform stress distributions, or both (e.g., Noda *et al.*, 2013). We show that this factor contributes as much as a factor of 3 overestimate to a factor of 3 underestimate of stress drops for different sources (Fig. 16d).

More broadly, the approach of interpreting corner frequencies in terms of a radius of a circle with the same source area, as inherent in the definition (5) of nondimensional corner frequency k, may benefit from revisiting, given the data of sufficient quality. It should be possible to use the information from the variation of corner frequencies and high-frequency fall-off over individual stations to determine the source shape and directivity, as done in second-moment methods. A potential distinguishing feature is the ratio of k^P/k^S. We find that the MA model (MA model 1) is the only model with k^P higher than k^S for most ζ (other than the smallest values) from the focal sphere (Fig. 9, Fig. S5). The other models, all of which have either directivity, and/or changing slip directions, and/or shapes different from circular, have a qualitatively different k distribution in which k values concentrate near small ζ and have much larger scatter for larger ζ (Figs. S6–S11), suggesting that the MA model may have a unique spectral signature over the focal sphere. Another possibility to consider is the potential to improve the fit using an intermediate slope to the spectrum (Denolle and Shearer, 2016); we will explore this point, which might be particularly relevant for rupture models with large aspect ratios, in future work.

Need to conduct synthetic tests with realistic path and site effects

We emphasize that the second-moment approach requires higher-quality data and an excellent understanding of the path and site effects to work well because it uses durations for individual stations to estimate second moments. The main reason for averaging all stations in the spectral-fitting approach and using a single average value of k is the need to separate source effects from path and site effects using limited data. Hence, it would be important to conduct synthetic tests similar to ours while accounting for various path and site effects, including scattering and multipathing, as well as variations in station coverage and various sources of noise in seismograms. As a step in that direction, we analyze estimated stress drops with a smaller subset of stations, 8 rather than 16 (Fig. 19d) for the source models without a hole. The results demonstrate that the reduction in the number of stations does not change the spread of the inferred stress drops for the spectral approach (Fig. 19b, c), but does increase the spread for the second-moment approach (Fig. 19a). The MAD of *bias* for the second-moment approach increases from 0.21 to 0.36 (Table 5), corresponding to an extension of the estimated stress-drop scattering from 62%–162% to 44%–229%. We expect an even larger scatter in stress-drop estimates for the number of stations less than eight, which is common in microseismicity studies. This simple example demonstrates the need to conduct synthetic studies with the realistic number of stations as well as path effects, source effects, and noise.

Mild dependence of stress-drop estimates on the abruptness of rupture arrest

All earthquake sources arrest in a region of VS friction, whereas on natural faults earthquakes can arrest at unbreakable boundaries of secondary faults as well as within the larger seismogenic region due to insufficient stress. We have tested the effect of rupture arrest on our MA models, creating a model (MA model 2) that has a very similar moment-rate function to the source with the unbreakable barrier from Madariaga (1976) and another model (MA model 3) that has a much more gradual arrest than the base case. We find that the abruptness of the arrest has a smaller effect on stress-drop estimates, including their mean and scatter, compared to other source properties such as directivity, elongated shape, and a patchy rupture (similar to the ring-like sources).

Possibility of systematic bias with depth due to network geometry

One important finding of this study is that the network geometry combined with the features of earthquake source may induce nonrandom, systematic bias in stress drops with depth. For example, there is a strong variation from slight stress-drop overestimate at shallow depths to significant underestimate deeper for the ELLI asymmetric source (ELLI A/I = 4 model 7; Fig. 16, middle row) for spectral fitting with S wave and n = 2. The cases for $D/H \leq 0.5$ are appropriate for crustal earthquakes (focal depth ≤ 21.2 km). If all observed events had this source mechanism, then the observational inference of depth-independent stress drop of 3 MPa would actually imply that the stress drops systematically vary from about that value (3/1.1 = 2.7 MPa) at shallow depth of $D = H/8 \sim 5$ km to three times larger value (9 MPa) at depth of $D = H/2 \sim 20$ km, to even larger values, up to 30 MPa, at larger depth. A similar—but much weaker—systematic trend with depth in stress-drop estimates exists even for all our sources put together (Fig. 17).

Importance of identifying most common microearthquake sources and their characteristics

Our findings suggest that the interpretation of stress-drop estimates significantly depends on what are the most common earthquake source models for microseismic events. Even in the ideal case of a known path as pursued in this study, both the second moment and spectral methods significantly underestimate the stress drop of ring-like ruptures, a conclusion which would hold for all partial, spotty ruptures. Spectral approaches based on P waves significantly underestimate stress drops for all our asymmetric and elongated sources, by a factor of 10 or more, implying that the average estimated stress drops for small events of 1–10 MPa may be a significant underestimate, with the actual stress drops being much higher; values in the range of 30–90 MPa would be more consistent with selected careful studies such as the study of Parkfield repeaters (Dreger *et al.*, 2007; Abercrombie, 2014). For the spectral methods and horizontally elongated sources, a limited network extent can introduce (and hence hide) systematic depth-dependent trends in stress drops.

Yet such asymmetric, elongated, patchy ruptures can be quite common or even dominating on natural faults. The very presence of microseismicity implies either heterogeneity on a larger fault segment or existence of secondary faults of a small extent. In the case of heterogeneity, earthquake ruptures are unlikely to spread equally in all directions with a constant rupture speed reaching a perfect circle, as assumed in MA models. The ruptures would follow places with the lowest fault strength and the highest fault stress, which would be governed by fault heterogeneity and/or locations of stress concentrations. Stress concentrations are likely to be band-like, following transitions in friction properties or the arrest boundaries of previous events. Transitions in properties may tend to be horizontal or semihorizontal due to earth layering and increases in normal stress and temperature with depth. All faults are likely to have local variations in normal stress due to roughness, as assumed in a simplified way in our asperity family. Small secondary immature faults especially are likely to be quite rough, with strong variations in normal stress, and noncircular, with nucleation at fault boundaries which promote stress concentrations. Indeed, detailed studies of small rupture events indicate a significant degree of complexity, including heterogeneous patchy stress drop (Dreger *et al.*, 2007) and most events having rupture directivity (Ross *et al.*, 2020). As such, elongated asymmetric ruptures like our ELLI A/I = 4 model 7 or partial ruptures like our ring-like sources may be more common than symmetric circular MA sources.

Hence, to better constrain stress drops and other properties of microseismicity, we need more understanding of which types of earthquake sources are common on natural faults and at what depth. For example, the best value of average k to use in spectral methods would significantly depend on which type of sources dominate on natural faults. An important path forward is to conduct earthquake sequence simulations with realistic fault constitutive descriptions, under physically plausible conditions, and in the presence of realistic fault heterogeneity, to understand the range of physically plausible microseismicity sources and the impact of their dynamics on radiation patterns and stress-drop estimates. Although it is likely that this would lead to a large variety of microseismicity sources, it is also possible that these sources would cluster in characteristic groups with similar radiation patterns, which would enable more detailed analyses of the seismograms with second-moment, spectral, and other methods.

DATA AND RESOURCES

All data used in this article are either from our simulations or from published sources listed in the references. Some calculations and plots were made using MATLAB (https://www.mathworks.com/products/matlab.html). Some plots were made using the Generic Mapping Tools (GMT) version 4.5 (www.soest.hawaii.edu/gmt; Wessel and Smith, 1998). Some plots were modified by Illustrator CC which is available at https://www.adobe.com/tw/products/illustrator.html. All websites were last accessed in December 2024. In supplemental material, we provide all simulated source models that are analyzed in this article (and listed in Table 3) in terms of their slip-rate variation in space and time as well as our MATLAB code for reading the slip-rate functions (STF.zip). Table S1 demonstrates the estimates of source parameters for all models.

DECLARATION OF COMPETING INTERESTS

The authors acknowledge that there are no conflicts of interest recorded.

ACKNOWLEDGMENTS

This study was supported by the National Science Foundation (NSF; Grant Numbers 1724686 and 2139331). It was also supported by the Taiwan Earthquake Research Center (TEC), funded through the National Science and Technology Council (NSTC) with Grant

Numbers 105-2917-I-564-015-, 108-2116-M-008-025-MY2, and 113-2116-M-008-007-. The TEC number for this article is 00196. This work is financially supported by the "Earthquake-Disaster & Risk Evaluation and Management Center, E-DREaM" from The Featured Areas Research Center Program within the framework of the Higher Education Sprout Project by the Ministry of Education (MOE) in Taiwan. The data used are listed in the references, tables, and supplemental material. The authors are grateful for the thorough reviews and suggestions from Rachel Abercrombie, Bill Ellsworth, and an anonymous reviewer, which served to significantly strengthen the article.

REFERENCES

Abercrombie, R. E. (1995). Earthquake source scaling relationships from −1 to 5 ML using seismograms recorded at 2.5-km depth, *J. Geophys. Res.* **100,** no. B12, 24,015–24,036.

Abercrombie, R. E. (2014). Stress drops of repeating earthquakes on the San Andreas Fault at Parkfield, *Geophys. Res. Lett.* **41,** no. 24, 8784–8791.

Abercrombie, R. E. (2015). Investigating uncertainties in empirical Green's function analysis of earthquake source parameters, *J. Geophys. Res.* **120,** no. 6, 4263–4277.

Abercrombie, R. E. (2021). Resolution and uncertainties in estimates of earthquake stress drop and energy release, *Philo. Trans. Roy. Soc. A* **379,** no. 2196, 20200131, doi: 10.1098/rsta.2020.0131.

Abercrombie, R. E., S. Bannister, A. Pancha, T. H. Webb, and J. J. Mori (2001). Determination of fault planes in a complex aftershock sequence using two-dimensional slip inversion, *Geophys. J. Int.* **146,** no. 1, 134–142.

Abercrombie, R. E., S. Bannister, J. Ristau, and D. Doser (2017). Variability of earthquake stress drop in a subduction setting, the Hikurangi Margin, New Zealand, *Geophys. J. Int.* doi: 10.1093/gji/ggw393.

Abercrombie, R. E., X. Chen, and J. Zhang (2020). Repeating earthquakes with remarkably repeatable ruptures on the San Andreas Fault at Parkfield, *Geophys. Res. Lett.* **47,** no. 23, e2020GL089820, doi: 10.1029/2020GL089820.

Aki, K. (1967). Scaling law of seismic spectrum, *J. Geophys. Res.* **72,** no. 4, 1217–1231.

Aki, K., and P. G. Richards (2002). *Quantitative Seismology*, Second Ed., University Science Books, Sausalito, California, 700 pp.

Allmann, B. P., and P. M. Shearer (2007). Spatial and temporal stress drop variations in small earthquakes near Parkfield, California, *J. Geophys. Res.* **112,** no. B4, doi: 10.1029/2006JB004395.

Allmann, B. P., and P. M. Shearer (2009). Global variations of stress drop for moderate to large earthquakes, *J. Geophys. Res.* **114,** no. B1, doi: 10.1029/2008JB005821.

Allmann, B. P., P. M. Shearer, and E. Hauksson (2008). Spectral discrimination between quarry blasts and earthquakes in southern California, *Bull. Seismol. Soc. Am.* **98,** no. 4, 2073–2079.

Backus, G., and M. Mulcahy (1976). Moment tensors and other phenomenological descriptions of seismic sources—I. Continuous displacements, *Geophys. J. Int.* **46,** no. 2, 341–361.

Backus, G. E. (1977). Interpreting the seismic glut moments of total degree two or less, *Geophys. J. Int.* **51,** no. 1, 1–25.

Baltay, A., S. Ide, G. Prieto, and G. Beroza (2011). Variability in earthquake stress drop and apparent stress, *Geophys. Res. Lett.* **38,** no. 6, doi: 10.1029/2011GL046698.

Barbot, S., N. Lapusta, and J. P. Avouac (2012). Under the hood of the earthquake machine: Toward predictive modeling of the seismic cycle, *Science* **336,** no. 6082, 707–710.

Ben-Zion, Y., and J. R. Rice (1997). Dynamic simulations of slip on a smooth fault in an elastic solid, *J. Geophys. Res.* **102,** no. B8, 17,771–17,784.

Boatwright, J. (1980). A spectral theory for circular seismic sources; simple estimates of source dimension, dynamic stress drop, and radiated seismic energy, *Bull. Seismol. Soc. Am.* **70,** no. 1, 1–27.

Brune, J. (1971). Correction [to "Tectonic stress and the spectra, of seismic shear waves from earthquakes"], *J. Geophys. Res.* **76,** no. 20, 5002–5002.

Brune, J. N. (1970). Tectonic stress and the spectra of seismic shear waves from earthquakes, *J. Geophys. Res.* **75,** no. 26, 4997–5009.

Chang, H., R. E. Abercrombie, N. Nakata, C. N. Pennington, K. B. Kemna, E. S. Cochran, and R. M. Harrington (2023). Quantifying site effects and their influence on earthquake source parameter estimations using a dense array in Oklahoma, *J. Geophys. Res.* **128,** e2023JB027144, doi: 10.1029/2023JB027144.

Chen, K. H., I. Chen, and A. Kim (2016). Can slip heterogeneity be linked to earthquake recurrence? *Geophys. Res. Lett.* **43,** no. 13, 6916–6923.

Chen, T., and N. Lapusta (2009). Scaling of small repeating earthquakes explained by interaction of seismic and aseismic slip in a rate and state fault model, *J. Geophys. Res.* **114,** no. B1, doi: 10.1029/2008JB005749.

Demuth, A., N. Tjåland, and L. Ottemöller (2019). Earthquake source parameters in Norway determined with empirical Green's functions, *J. Seismol.* **23,** 715–724.

Denolle, M. A., and P. M. Shearer (2016). New perspectives on self-similarity for shallow thrust earthquakes, *J. Geophys. Res.* **121,** no. 9, 6533–6565.

Dieterich, J. (1994). A constitutive law for rate of earthquake production and its application to earthquake clustering, *J. Geophys. Res.* **99,** no. B2, 2601–2618.

Dieterich, J. H. (1979). Modeling of rock friction: 1. Experimental results and constitutive equations, *J. Geophys. Res.* **84,** no. B5, 2161–2168.

Dieterich, J. H. (2007). Applications of rate-and state-dependent friction to models of fault slip and earthquake occurrence, *Earthq. Seismol.* **4,** 107–129.

Dreger, D., R. M. Nadeau, and A. Chung (2007). Repeating earthquake finite source models: Strong asperities revealed on the San Andreas Fault, *Geophys. Res. Lett.* **34,** no. 23, doi: 10.1029/2007GL031353.

Ellsworth, W. L., and F. Bulut (2018). Nucleation of the 1999 Izmit earthquake by a triggered cascade of foreshocks, *Nature Geosci.* **11,** no. 7, 531–535.

Ellsworth, W. L., F. Waldhauser, and A. Cole (2000). A new view of the San Andreas Fault: Implications for earthquake interaction at Parkfield (ex-tended abstract), *International School of Geophysics*, Erice, Sicily.

Eshelby, J. D. (1957). The determination of the elastic field of an ellipsoidal inclusion, and related problems, *Proc. Math. Phys. Sci.* **241,** no. 1226, 376–396.

Fan, W., and J. J. McGuire (2018). Investigating microearthquake finite source attributes with IRIS community wavefield demonstration experiment in Oklahoma, *Geophys. J. Int.* **214,** no. 2, 1072–1087.

Frankel, A., and H. Kanamori (1983). Determination of rupture duration and stress drop for earthquakes in southern California, *Bull. Seismol. Soc. Am.* **73,** no. 6A, 1527–1551.

Gibowicz, S. J., R. P. Young, S. Talebi, and D. J. Rawlence (1991). Source parameters of seismic events at the underground research laboratory in Manitoba, Canada: Scaling relations for events with moment magnitude smaller than −2, *Bull. Seismol. Soc. Am.* **81,** no. 4, 1157–1182.

Hanks, T. C. (1979). b values and ω− γ seismic source models: Implications for tectonic stress variations along active crustal fault zones and the estimation of high-frequency strong ground motion, *J. Geophys. Res.* **84,** no. B5, 2235–2242.

Hanks, T. C., and M. Wyss (1972). The use of body-wave spectra in the determination of seismic-source parameters, *Bull. Seismol. Soc. Am.* **62,** no. 2, 561–589.

Haskell, N. A. (1964). Total energy and energy spectral density of elastic wave radiation from propagating faults, *Bull. Seismol. Soc. Am.* **54,** no. 6A, 1811–1841.

Helmstetter, A., and B. E. Shaw (2009). Afterslip and aftershocks in the rate-and-state friction law, *J. Geophys. Res.* **114,** no. B1, doi: 10.1029/2007JB005077.

Hough, S. E. (1997). Empirical Green's function analysis: Taking the next step, *J. Geophys. Res.* **102,** no. B3, 5369–5384.

Ide, S., and G. C. Beroza (2001). Does apparent stress vary with earthquake size? *Geophys. Res. Lett.* **28,** no. 17, 3349–3352.

Ide, S., G. C. Beroza, S. G. Prejean, and W. L. Ellsworth (2003). Apparent break in earthquake scaling due to path and site effects on deep borehole recordings, *J. Geophys. Res.* **108,** no. B5, doi: 10.1029/2001JB001617.

Ide, S., M. Matsubara, and K. Obara (2004). Exploitation of high-sampling Hi-net data to study seismic energy scaling the aftershocks of the 2000 Western Tottori, Japan, earthquake, *Earth Planets Space* **56,** no. 9, 859–871.

Imanishi, K., and M. Takeo (1998). Estimates of fault dimensions for small earthquakes using stopping phases, *Geophys. Res. Lett.* **25,** no. 15, 2897–2900.

Imanishi, K., and M. Takeo (2002). An inversion method to analyze rupture processes of small earthquakes using stopping phases, *J. Geophys. Res.* **107,** no. B3, ESE 2-1–ESE 2-16.

Irikura, K., and K. Kamae (1994). Estimation of strong ground motion in broad-frequency band based on a seismic source scaling model and an empirical Green's function technique, *Ann. Geogr.* **37,** 1721–1743.

Jiang, J., and Y. Fialko (2016). Reconciling seismicity and geodetic locking depths on the Anza section of the San Jacinto fault, *Geophys. Res. Lett.* **43,** no. 20, 10,663–10,671.

Jiang, J., and N. Lapusta (2016). Deeper penetration of large earthquakes on seismically quiescent faults, *Science* **352,** no. 6291, 1293–1297.

Kanamori, H., and D. L. Anderson (1975). Theoretical basis of some empirical relations in seismology, *Bull. Seismol. Soc. Am.* **65,** no. 5, 1073–1095.

Kaneko, Y., N. Lapusta, and J. P. Ampuero (2008). Spectral element modeling of spontaneous earthquake rupture on rate and state faults: Effect of velocity-strengthening friction at shallow depths, *J. Geophys. Res.* **113,** no. B9, doi: 10.1029/2007JB005553.

Kaneko, Y., and P. M. Shearer (2014). Seismic source spectra and estimated stress drop derived from cohesive-zone models of circular subshear rupture, *Geophys. J. Int.* **197,** no. 2, 1002–1015.

Kaneko, Y., and P. M. Shearer (2015). Variability of seismic source spectra, estimated stress drop, and radiated energy, derived from cohesive-zone models of symmetrical and asymmetrical circular and elliptical ruptures, *J. Geophys. Res.* **120,** no. 2, 1053–1079.

Kim, A., D. S. Dreger, T. A. Taira, and R. M. Nadeau (2016). Changes in repeating earthquake slip behavior following the 2004 Parkfield main shock from waveform empirical Green's functions finite-source inversion, *J. Geophys. Res.* **121,** no. 3, 1910–1926.

Lanza, V., D. Spallarossa, M. Cattaneo, D. Bindi, and P. Augliera (1999). Source parameters of small events using constrained deconvolution with empirical Green's functions, *Geophys. J. Int.* **137,** no. 3, 651–662.

Lapusta, N., and Y. Liu (2009). Three-dimensional boundary integral modeling of spontaneous earthquake sequences and aseismic slip, *J. Geophys. Res.* **114,** no. B9, doi: 10.1029/2008JB005934.

Lapusta, N., and J. R. Rice (2003). Nucleation and early seismic propagation of small and large events in a crustal earthquake model, *J. Geophys. Res.* **108,** no. B4, doi: 10.1029/2001JB000793.

Lapusta, N., J. R. Rice, Y. Ben-Zion, and G. Zheng (2000). Elastodynamic analysis for slow tectonic loading with spontaneous rupture episodes on faults with rate-and state-dependent friction, *J. Geophys. Res.* **105,** no. B10, 23,765–23,789.

Lay, T., and T. C. Wallace (1995). *Modern Global Seismology*, Academic Press, San Diego, California.

Lin, Y. Y., and N. Lapusta (2018). Microseismicity simulated on asperity-like fault patches: On scaling of seismic moment with duration and seismological estimates of stress drops, *Geophys. Res. Lett.* **45,** no. 16, 8145–8155.

Lin, Y. Y., K. F. Ma, H. Kanamori, T. R. Song, N. Lapusta, and V. C. Tsai (2016). Evidence for non-self-similarity of microearthquakes recorded at a Taiwan borehole seismometer array, *Geophys. J. Int.* **206,** no. 2, 757–773.

Lin, Y. Y., K. F. Ma, and V. Oye (2012). Observation and scaling of microearthquakes from the Taiwan Chelungpu-fault borehole seismometers, *Geophys. J. Int.* **190,** nol. 1, 665–676.

Liu, M., Y. Huang, and J. Ritsema (2023). Characterizing multisubevent earthquakes using the Brune source model, *Bull. Seismol. Soc. Am.* **113,** no. 2, 577–591.

Lui, S. K., and N. Lapusta (2016). Repeating microearthquake sequences interact predominantly through postseismic slip, *Nat. Commun.* **7,** no. 1, 13,020.

Madariaga, R. (1976). Dynamics of an expanding circular fault, *Bull. Seismol. Soc. Am.* **66,** no. 3, 639–666.

Madariaga, R. (1979). On the relation between seismic moment and stress drop in the presence of stress and strength heterogeneity, *J. Geophys. Res.* **84,** no. B5, 2243–2250.

Marques, R., C. Bouville, K. Bouatouch, and J. Blat (2019). Extensible spherical Fibonacci grids, *IEEE Trans. Vis. Comput. Graph.* **27,** no. 4, 2341–2354.

McGuire, J. J. (2004). Estimating finite source properties of small earthquake ruptures, *Bull. Seismol. Soc. Am.* **94,** no. 2, 377–393.

McGuire, J. J. (2017). A MATLAB toolbox for estimating the second moments of earthquake ruptures, *Seismol. Res. Lett.* **88,** no. 2A, 371–378.

McGuire, J. J., and Y. Kaneko (2018). Directly estimating earthquake rupture area using second moments to reduce the uncertainty in stress drop, *Geophys. J. Int.* **214,** no. 3, 2224–2235.

McGuire, J. J., L. Zhao, and T. H. Jordan (2001). Teleseismic inversion for the second degree moments of earthquake space–time distributions, *Geophys. J. Int.* **145,** no. 3, 661–678.

McGuire, J. J., L. Zhao, and T. H. Jordan (2002). Predominance of unilateral rupture for a global catalog of large earthquakes, *Bull. Seismol. Soc. Am.* **92,** no. 8, 3309–3317.

Miyake, H., T. Iwata, and K. Irikura (2003). Source characterization for broadband ground-motion simulation: Kinematic heterogeneous source model and strong motion generation area, *Bull. Seismol. Soc. Am.* **93,** no. 6, 2531–2545.

Mori, J., R. E. Abercrombie, and H. Kanamori (2003). Stress drops and radiated energies of aftershocks of the 1994 Northridge, California, earthquake, *J. Geophys. Res.* **108,** no. B11, doi: 10.1029/2001JB000474.

Noda, H., N. Lapusta, and H. Kanamori (2013). Comparison of average stress drop measures for ruptures with heterogeneous stress change and implications for earthquake physics, *Geophys. J. Int.* **193,** no. 3, 1691–1712.

O'Neill, M. E. (1984). Source dimensions and stress drops of small earthquakes near Parkfield, California, *Bull. Seismol. Soc. Am.* **74,** no. 1, 27–40.

Oye, V., H. Bungum, and M. Roth (2005). Source parameters and scaling relations for mining-related seismicity within the Pyhasalmi ore mine, Finland, *Bull. Seismol. Soc. Am.* **95,** no. 3, 1011–1026.

Pennington, C. N., H. Chang, J. L. Rubinstein, R. E. Abercrombie, N. Nakata, T. Uchide, and E. S. Cochran (2022). Quantifying the sensitivity of microearthquake slip inversions to station distribution using a dense nodal array, *Bull. Seismol. Soc. Am.* **112,** no. 3, 1252–1270.

Prieto, G. A., R. L. Parker, F. L. Vernon, P. M. Shearer, D. J. Thomson, R. Abercrombie, and A. McGarr (2006). Uncertainties in earthquake source spectrum estimation using empirical Green functions, in *Earthquakes: Radiated Energy and the Physics of Faulting*, Geophysical Monograph Series, R. Abercrombie, A. McGarr, G. Di Toro, and H. Kanamori (Editor), Vol. 170, American Geophysical Union, Washington, DC, 69–74.

Prieto, G. A., P. M. Shearer, F. L. Vernon, and D. Kilb (2004). Earthquake source scaling and self-similarity estimation from stacking P and S spectra, *J. Geophys. Res.* **109,** no. B8, doi: 10.1029/2004JB003084.

Rice, J. R. (1993). Spatio-temporal complexity of slip on a fault, *J. Geophys. Res.* **98,** no. B6, 9885–9907.

Rice, J. R., and A. L. Ruina (1983). Stability of steady frictional slipping, *J. Appl. Mech.* **50,** no. 2, 343–349.

Ross, Z. E., D. T. Trugman, K. Azizzadenesheli, and A. Anandkumar (2020). Directivity modes of earthquake populations with unsupervised learning, *J. Geophys. Res.* **125,** no. 2, e2019JB018299, doi: 10.1029/2019JB018299.

Rubin, A. M., and J. P. Ampuero (2005). Earthquake nucleation on (aging) rate and state faults, *J. Geophys. Res.* **110,** no. B11, doi: 10.1029/2005JB003686.

Ruina, A. (1983). Slip instability and state variable friction laws, *J. Geophys. Res.* **88,** no. B12, 10,359–10,370.

Sato, T., and T. Hirasawa (1973). Body wave spectra from propagating shear cracks, *J. Phys. Earth* **21,** no. 4, 415–431.

Schaff, D. P., G. H. Bokelmann, G. C. Beroza, F. Waldhauser, and W. L. Ellsworth (2002). High-resolution image of Calaveras fault seismicity, *J. Geophys. Res.* **107,** no. B9, ESE 5-1–ESE 5-1.

Shearer, P. M., R. E. Abercrombie, and D. T. Trugman (2022). Improved stress drop estimates for M 1.5 to 4 earthquakes in southern California from 1996 to 2019, *J. Geophys. Res.* **127,** no. 7, e2022JB024243, doi: 10.1029/2022JB024243.

Shearer, P. M., R. E. Abercrombie, D. T. Trugman, and W. Wang (2019). Comparing EGF methods for estimating corner frequency and stress drop from P wave spectra, *J. Geophys. Res.* **124,** no. 4, 3966–3986.

Shearer, P. M., G. A. Prieto, and E. Hauksson (2006). Comprehensive analysis of earthquake source spectra in southern California, *J. Geophys. Res.* **111,** no. B6, doi: 10.1029/2005JB003979.

Shimmoto, S. (2022). Stress drop estimates for small to moderate earthquakes in Tohoku, Japan considering rupture geometry, speed, and directivity, *J. Geophys. Res.* **127,** no. 8, e2022JB025157, doi: 10.1029/2022JB025157.

Silver, P. (1983). Retrieval of source-extent parameters and the interpretation of corner frequency, *Bull. Seismol. Soc. Am.* **73,** no. 6A, 1499–1511.

Silver, P. G., and T. H. Jordan (1983). Total-moment spectra of fourteen large earthquakes, *J. Geophys. Res.* **88,** no. B4, 3273–3293.

Swinbank, R., and R. J. Purser (2006). Fibonacci grids: A novel approach to global modelling, *Q. J. R. Meteorol. Soc.* **132,** no. 619, 1769–1793.

Trugman, D. T., and P. M. Shearer (2017). Application of an improved spectral decomposition method to examine earthquake source scaling in Southern California, *J. Geophys. Res.* **122,** no. 4, 2890–2910.

Uchide, T., and K. Imanishi (2016). Small earthquakes deviate from the omega-square model as revealed by multiple spectral ratio analysis, *Bull. Seismol. Soc. Am.* **106,** no. 3, 1357–1363.

Van Houtte, C., and M. Denolle (2018). Improved model fitting for the empirical Green's function approach using hierarchical models, *J. Geophys. Res.* **123,** no. 4, 2923–2942.

Walter, W. R., S. H. Yoo, K. Mayeda, and R. Gök (2017). Earthquake stress via event ratio levels: Application to the 2011 and 2016 Oklahoma seismic sequences, *Geophys. Res. Lett.* **44,** no. 7, 3147–3155.

Wang, Y., and S. M. Day (2017). Seismic source spectral properties of crack-like and pulse-like modes of dynamic rupture, *J. Geophys. Res.* **122,** no. 8, 6657–6684.

Wessel, P., and W. H. Smith (1998). New, improved version of Generic Mapping Tools released, *EOS., Trans. AGU* **79,** no. 47, 579.

Wu, Q., X. Chen, and R. E. Abercrombie (2019). Source complexity of the 2015 Mw 4.0 Guthrie, Oklahoma earthquake, *Geophys. Res. Lett.* **46,** no. 9, 4674–4684.

Yamada, T., J. J. Mori, S. Ide, R. E. Abercrombie, H. Kawakata, M. Nakatani, Y. Iio, and H. Ogasawara (2007). Stress drops and radiated seismic energies of microearthquakes in a South African gold mine, *J. Geophys. Res.* **112,** no. B3, doi: 10.1029/2006JB004553.

Ye, L., T. Lay, H. Kanamori, and L. Rivera (2016a). Rupture characteristics of major and great (Mw≥ 7.0) megathrust earthquakes from 1990 to 2015: 1. Source parameter scaling relationships, *J. Geophys. Res.* **121,** no. 2, 826–844.

Ye, L., T. Lay, H. Kanamori, and L. Rivera (2016b). Rupture characteristics of major and great (Mw≥ 7.0) megathrust earthquakes from 1990 to 2015: 2. Depth dependence, *J. Geophys. Res.* **121,** no. 2, 845–863.

Manuscript received 25 June 2024
Published online 4 March 2025